

1
2
3 **REVISION 1**

4 **Experimental investigation into the substitution mechanisms and solubility of**
5 **Ti in garnet**

6 **Michael R. Ackerson^{1,2}, E. Bruce Watson¹, Nicholas D. Tailby¹, Frank S. Spear¹**

7 ¹Department of Earth and Environmental Sciences, Rensselaer Polytechnic Institute,
8 Troy, NY, 12180

9 ²Geophysical Laboratory, Carnegie Institution of Washington, Washington, D.C.,
10 20015

11 **Abstract**

12
13 Garnet is a common and important mineral in metamorphic systems, but the
14 mechanisms by which it incorporates Ti— one of the major elements in the crust—
15 are not well constrained. This study draws upon garnets synthesized at a range of
16 temperatures and pressures to understand Ti solubility and the substitution
17 mechanisms that govern its incorporation into garnet at eclogite and granulite facies
18 conditions. Garnets from these synthesis experiments can incorporate up to several
19 wt. % TiO₂. Comparison of Ti content with deficits in Al and Si in garnet indicates
20 that Ti is incorporated by at least two substitution mechanisms (${}^{\text{VI}}\text{Ti}^{4+} + {}^{\text{VI}}\text{M}^{2+} \rightleftharpoons$
21 $2{}^{\text{VI}}\text{Al}^{3+}$, and ${}^{\text{VI}}\text{Ti}^{4+} + {}^{\text{IV}}\text{Al}^{3+} \rightleftharpoons {}^{\text{VI}}\text{Al}^{3+} + {}^{\text{IV}}\text{Si}^{4+}$). Increasing Ti solubility is correlated with
22 increasing Ca and Fe/Mg ratios in garnet, clinopyroxene and melt. The complexity of
23 the substitution mechanisms involved in Ti solubility in garnet make practical Ti-in-
24 garnet thermobarometry infeasible at present. However, a model fit to Ti
25 partitioning between garnet and melt can be used to predict melt compositions in
26 high grade metamorphic systems. Additionally, the solubility and substitution
27 mechanisms described here can help explain the presence of crystallographically-
28 aligned rutile needles in high grade metamorphic systems.

29

30

31

Introduction

32

33

34

35

36

37

38

39

40

41

42

43

44

45

46

47

48

49

50

51

52

53

Garnet is a common mineral in the crust and mantle, and its chemical composition is crucial to our understanding of the chemical, physical and temporal evolution of the earth. Its utility extends from its major-element composition [e.g. Fe/Mg exchange between garnet and other phases used in thermobarometry (Råheim and Green 1974; Ellis and Green 1979; Krogh 1988; Pattison and Newton 1989)] to its trace elements [e.g. Sm-Nd dating, Y zoning (Lanzirotti 1995; Baxter et al. 2002; Thöni 2002; Pyle and Spear 2003)]. Still, it behooves geoscientists to develop new garnet-based petrogenetic tools to better constrain our understanding of metamorphic processes. While extensive work has been performed developing and applying garnet-based petrogenetic tools, the utility of Ti in garnet remains unclear. The fact that Ti activity is often buffered in natural metamorphic systems by the presence of rutile—combined with its typically trace or minor abundance in most garnets—makes Ti a potentially useful element for developing novel petrogenetic tools involving garnet. However, its utility is currently hampered by our limited understanding of the mechanism of Ti substitution into garnet and the factors influencing its solubility.

The generalized chemical formula for garnets is $(X_3Y_2Z_3O_{12})$. While there are over 29 naturally-occurring and hypothetical garnet end members, the majority of crustal garnets lie within the pyrospite and ugrandite groups (Locock 2008). The former is typified by octahedral Al and the latter by dodecahedral Ca. The X site is a dodecahedral site containing divalent cations Ca, Fe, Mg, and Mn (denoted

54 generically as M^{2+}). The octahedral Y site contains trivalent Al and Fe^{3+} , and the
55 tetrahedral Z site is primarily tetravalent Si. Most crustal garnets maintain a
56 divalent-trivalent-tetravalent ratio of 3:2:3, but the addition of Ti to the crystal
57 structure of garnet has been demonstrated to move these ratios out of stoichiometry
58 (Huggins et al., 1977(2), sources therein).

59 Although site occupancy of most major elements in garnet is well
60 understood, Ti coordination and potential substitution mechanisms have been a
61 subject of considerable discussion beginning as early as Zedlitz (1933). Several
62 studies have suggested— based on the hypothetical end-member configurations of
63 melanite and schorlomite garnets— that Ti^{4+} incorporation occurs primarily on the
64 tetrahedral Z site in garnet (Armbruster and Geiger 1993; Scordari et al. 2003).
65 Conversely— based on intra-crystalline chemical variations (Gwalani et al. 2000;
66 Chakhmouradian and McCammon 2005; Grew et al. 2013; Proyer et al. 2013) and
67 XANES analyses of schorlomite garnets (Waychunas 1987)— others have suggested
68 that Ti incorporation occurs primarily on the octahedral Y site. Substitution of Ti^{4+}
69 onto the tetrahedral site in garnet can be achieved through a simple $Ti^{4+} \rightleftharpoons Si^{4+}$
70 substitution with Si^{4+} . However, octahedral Ti^{4+} requires a charge-balancing
71 mechanism for Al^{3+} . Alternatively, Ti^{3+} could be incorporated into the octahedral
72 site, although most studies suggest Ti^{3+} in naturally-occurring garnets or terrestrial
73 melts is negligible (Huggins et al. 1977; Gwalani et al. 2000; Chakhmouradian and
74 McCammon 2005; Krawczynski et al. 2009; Grew et al. 2013).

75 While most continental metamorphic garnets contain minor to trace
76 amounts of Ti, crystallographically-aligned rutile needles from high-grade

77 metamorphic garnets (primarily eclogites, granulites and mantle xenoliths) indicate
78 elevated Ti concentrations (up to several weight % TiO₂) at high temperatures and
79 pressures. The commonly accepted petrogenetic theory behind the occurrence of
80 these rutile needles involves the retrogressive exsolution of rutile from the garnet
81 crystal lattice during exhumation to the surface (Ye et al. 2000; Alifirova et al. 2012;
82 Ague et al. 2013; Proyer et al. 2013).

83 Laboratory synthesis of garnets at elevated temperatures and pressures
84 enables observation of Ti coordination and solubility systematics in garnets at
85 geologic conditions where the Ti signature in natural garnets would probably
86 experience changes upon exhumation (as suggested by exsolved rutile/ilmenite
87 crystals in some high grade garnets). High Ti concentrations in experimental garnets
88 could bolster observations from natural systems and serve as a novel means to
89 identify high-grade metamorphic signatures where the other indicators (diamond or
90 coesite inclusions) may be absent. Furthermore, the controlled environment of
91 experimental synthesis allows for direct observations of the thermal, barometric
92 and chemical controls on Ti coordination and concentration in garnet.

93 In this study we aim to demonstrate using experimentally-grown garnets
94 that incorporation of Ti occurs primarily on the octahedral site via multiple
95 substitution mechanisms. Ti partitioning between garnet and silicate melts can be
96 modelled using temperature and melt composition, while pressure appears to have
97 little effect on partitioning over the experimental range. Ti solubility of experimental
98 garnets at high pressures and temperatures correlates with the inferred solubility in
99 natural high grade garnets that contain crystallographically-aligned rutile needles.

100
101

Experimental

102 Experiments were performed in a piston-cylinder apparatus at Rensselaer
103 Polytechnic Institute. Rock powders and oxygen fugacity buffers were loaded into
104 opposite sides of two-chamber Ag capsules. Rock powders were juxtaposed against
105 the oxygen fugacity buffers and separated by Ag-Pd or Pd foil. The Ag capsule was
106 then loaded into a graphite-NaCl-Pyrex® assembly with MgO, Pyrex® and fired
107 pyrophyllite filler pieces (Fig. 1).

108 Three bulk compositions (Table 1) were selected based on the bulk
109 compositions from which garnets crystallize in a subducting oceanic slab. The
110 compositions include: a synthetic amphibolite (AMPH) based on the pillowed
111 greenstone amphibolite (Composition No. 4) of (Rapp and Watson 1995), a
112 synthetic global subducting sediment (GLOSS) of (Plank and Langmuir 1998), and a
113 natural basalt (SUNY MORB, Richter et al. 2003). Bulk compositions were then
114 doped with 5 wt. % TiO₂ and 1 wt. % ZrO₂ to ensure saturation of rutile and/or
115 ilmenite and zircon (respectively). Prior to running the experiments charges were
116 also doped with 10 wt.% H₂O to facilitate crystal nucleation and grain growth.
117 Experiments were performed over a range of temperatures, pressures and
118 compositions (Table 2, Fig. 2). All experiments performed in this study were
119 buffered at the fayalite-magnetite-quartz (FMQ) buffer. All buffers were checked at
120 the end of the experiments to assure they contained the assemblage fayalite +
121 magnetite + quartz. In some experiments the buffer assemblage was not FMQ, likely
122 because the buffer was depleted before experimental completion. These
123 experiments were repeated with new powders and larger volumes of buffer to

124 ensure the buffers were not depleted. Some experiments were also doped with <72
125 μm Gore Mountain garnet seeds (Wentorf 1956) as a surface for epitaxial garnet
126 growth to overcome the garnet nucleation barrier (Yoder and Tilley 1962).
127 Experimental duration was typically 48 hrs, although additional experiments were
128 performed at 24 and 72 hrs. Despite evidence for chemical zoning in garnets
129 (discussed below) the near-identical compositions of the rims of phases present
130 over multiple time scales suggests that experiments reach equilibrium over run
131 durations as short as 24 hrs (Table 2).

132 **Analytical procedure**

133
134 Chemical analyses of all experimental phases were performed using a
135 Cameca SX 100 electron probe microanalyzer (EPMA) at Rensselaer Polytechnic
136 Institute. The electron beam was operated at a 15 kV accelerating voltage and a 20
137 nA current with a 2 μm beam size. Ti in synthetic garnets was counted on Ti $K\alpha$ X-
138 rays using two large PET crystals with peak-measuring durations of 20 seconds. ZAF
139 corrections of the glass compositions were calculated assuming all analyses lower
140 than 100% were due to H from dissolved water. Garnet and clinopyroxene were
141 analyzed at their rims due to the existence of core-rim zoning in most experiments.
142 Several analyses were also performed at 10 kV to ensure the large activation volume
143 of the 15 kV beam was not generating significant secondary fluorescence from
144 proximal titaniferous phases.

145 **Secondary fluorescence**

146 Secondary fluorescence was a specific concern when analyzing Ti in garnet.
147 Secondary fluorescence of Ti occurs when Ti $K\alpha$ X-rays are generated in a phase

148 adjacent to (in this case ilmenite or rutile) the phase of interest (garnet) via
149 interaction between ilmenite/rutile and high energy X-rays generated within the
150 excitation volume of the incident electron beam. Secondary X-rays have been shown
151 to result in erroneously high apparent Ti contents in minerals and alloys at
152 distances greater than 100 μm from phase boundaries (Bastin et al. 1984, Feenstra
153 and Engi 1998, Wark and Watson 2006, Jercinovic et al. 2008). In particular,
154 Feenstra and Engi (1998) saw fluorescence in a garnet adjacent to ilmenite at a
155 distance greater than 40 μm .

156 The results of Feenstra and Engi (1998) could pose a significant problem for
157 analysis of Ti in experimental garnet due to the large number of ilmenite and rutile
158 inclusions in garnets (Fig. 4). However, the magnitude of secondary fluorescence
159 effects depends critically on the geometry of the contact between the two phases.
160 Feenstra and Engi (1998) conducted secondary fluorescence experiments using
161 polished slabs of garnet and ilmenite juxtaposed against each other in a plane
162 parallel to the direction of the incident beam, thus maximizing the amount of
163 ilmenite interacting with the electron beam (and secondary X-rays). This geometry
164 contrasts with that of most experimentally-grown garnets, which contain small (5
165 μm) ilmenite or rutile inclusions— meaning fewer secondary X-rays will interact
166 with the ilmenite/rutile than in the case of an infinite planar interface.

167 The magnitude of secondary fluorescence effects can be explored directly
168 with the EPMA on various target geometries, and also using the program PENEPMMA
169 ("Penetration and Energy Loss of Positrons and Electrons, Electron Probe
170 Microanalysis"; Fournelle 2007). Electron-probe analyses of garnet approaching an

195 and the Fe-Ti oxide phase(s). All garnets are primarily almandine with varying
196 amounts of grossular and pyrope components and < 5 % spessartine.
197 Clinopyroxenes are bladed with a maximum diameter of ~10 μm perpendicular to
198 the long axis. They are primarily hedenbergite composition with several weight %
199 Mg and Al (Table 5).

200 Both garnets and clinopyroxenes in most experiments are zoned from core-
201 rim. This is consistent with observations from other experimental studies at similar
202 temperatures (Råheim and Green 1974; Ellis and Green 1979; Pattison and Newton
203 1989) where low temperatures, highly viscous melt compositions and rapid mineral
204 growth surpass the ability of complete mineral-melt re-equilibration. The large size
205 of garnets allows for core-rim analysis of the chemical zoning. Garnets
206 systematically become more Fe, Ca, and Ti poor and Mg and Mn rich from core to
207 rim. The relatively small size of pyroxenes makes observing systematic zoning
208 difficult via EPMA, but generally there is rim-ward increase in Fe and Ca relative to
209 Mg, with no resolvable change in Ti. The small size and zoning within the pyroxenes
210 as well as the number of rutile and/or ilmenite inclusions made it difficult to obtain
211 consistent and meaningful analyses of pyroxenes in many run products.

212 All experiments were performed above the wet solidus of the bulk
213 compositions used for garnet synthesis as demonstrated by the presence of
214 quenched melt (glass) in all experiments. Glass compositions ranged from dacitic to
215 rhyolitic for all bulk compositions analyzed. Melt compositions were analyzed in
216 experiments that contained segregated melt pools large enough to be analyzed by
217 EPMA. However, most experimental glasses are too densely populated with mineral

218 inclusions or vapor bubbles to obtain meaningful chemical compositions. High
219 spatial densities of Ti-oxide minerals in the melt and the possibility of secondary
220 fluorescence increasing the measured Ti content of the melt cannot be discounted
221 (Hayden and Watson 2007). Analytical points were chosen in melt where no oxide
222 phases were present within 20 μm , although sub-surface inclusions could contribute
223 to the measured (apparent) Ti content of the melt.

224 While most experiments were performed for 48 hours, experiments were
225 also conducted for 24 and 72 hours to observe possible time-dependent effects on
226 the experimental results. The results of these experiments display negligible
227 compositional drift over the time interval (Table 3). The same phases are present in
228 all of these time series experiments at similar proportions. Additionally, garnets
229 analyzed using a 10 kV beam returned near-identical results to analyses using a 15
230 kV beam (Table 3).

231 Additionally, garnet and melt composition data from multiple experimental
232 studies (Rapp and Watson 1995; Tailby 2009; Qian and Hermann 2013) were
233 included with the data from this study in order to sample a wide compositional,
234 thermal and barometric range over which to observe chemical trends in garnet.
235 Oxygen normalization of garnet compositional data to an ideal 12 oxygen per
236 formula unit (a.p.f.u.) provides information on deviations from idealized garnet
237 chemistry. In ideal pyrospite and grossular garnets there are two moles of Al for
238 every mole of garnet, all of which exists on the octahedral site. If other elements
239 substitute onto the octahedral site the aluminum content will decrease in
240 stoichiometric proportion with the substituting cation. Similarly, there should only

241 be 3 total moles of the M^{2+} cations and 3 moles of Si. Deviations from ideal
242 stoichiometry are reported in table 3, and are defined as:

243
$$Al\ deficit = 2 - Al(apfu)$$

244
$$Si\ deficit = 3 - Si(apfu)$$

245
$$excess\ M^{2+}\ cations = \sum M^{2+}(apfu) - 3$$

246 The data reported in table 3 of garnet compositions are the averages of at least
247 six garnet analyses from each experiment near the rims of the garnets (see below
248 for discussion of garnet zoning). It is important to consider the magnitude of
249 analytical uncertainty (x-ray counting errors) of individual data points and actual
250 compositional variations within populations from a single experiment, and the role
251 these statistical aspects will have in interpreting relationships between elements in
252 garnets both within a single experiment and between experiments. The errors
253 associated with derived quantities (e.g., Al- and Si-deficit) are ultimately the errors
254 associated with measurement of Al and Si content in the garnets. For the EPMA
255 routine used in this study, the relative standard deviations ($RSD = 100 \frac{SE}{x}$, where SE
256 is the 1σ standard error of the measurement and x is the measured value of a given
257 element) of individual element measurements result in minimal errors in the
258 derived quantities (Si- and Al-deficit, excess cations) and are encompassed in the
259 error bars reported for the derived quantities (Table 3). Intra-experimental
260 variations in garnet composition are generally higher than the analytical error.
261 Ultimately, the intra-sample errors on elemental measurements have a
262 significant impact on the error bars on the derived quantities, in particular the
263 excess cation values. Error propagation of the intra-sample errors for the excess

264 cations can be approximated using the formula:

265 $SD(\text{excess } M^{2+}) = \sqrt{(SD_{Mg})^2 + (SD_{Fe})^2 + (SD_{Fe})^2 + (SD_{Mn})^2}$. This formula is a

266 minimum error on the excess M^{2+} cations because it neglects the correlation

267 coefficient between the variables which has been shown (Kohn and Spear 1991a,

268 1991b) to be important when estimating errors on normalized formulae. The

269 propagated errors on the excess M^{2+} values are often greater than the quantities

270 themselves. For example the calculated excess M^{2+} value for sample 15-AMPH is

271 0.08 ± 0.14 . In the same sample the Al deficit is 0.08 ± 0.02 . Combining multiple

272 sources of errors also makes it difficult to determine the proportions of substitution

273 mechanisms contributing to individual data points.

274 **Discussion**

275

276 Understanding the factors influencing Ti solubility in garnet is important for

277 interpreting crustal and mantle geochemical processes. In the following discussion

278 we aim to demonstrate, using garnets grown at eclogite- and granulite-facies

279 conditions, that (1) Ti incorporation must occur through multiple substitution

280 mechanisms onto the octahedral site, (2) Ti incorporation into garnet is influenced

281 by ^{VIII}Ca and is correlated with increases in Fe/Mg fractions in garnet, clinopyroxene

282 and the melt, (3) temperature, melt composition and garnet-melt K_D values can be

283 used to predict Ti concentrations in garnet, and (4) exsolution of rutile from high-

284 grade garnets can be explained using the substitution mechanisms observed in this

285 study and open system exchange between garnets and their mineral or melt matrix.

286 **Attainment of equilibrium**

287 The observation of chemical zoning in garnets and pyroxenes demonstrates
288 disequilibrium within the experimental assembly. Calibrations of the garnet-
289 clinopyroxene Fe-Mg exchange thermobarometer have noted zoning in garnets at
290 temperatures and pressures equivalent to our experimental conditions (Yoder and
291 Tilley 1962; Råheim and Green 1974). Reversal experiments (Pattison and Newton
292 1989) indicate that the rim compositions of non-reversed garnet and clinopyroxene
293 are closest to the equilibrium value. By this logic, zoned minerals in our experiments
294 will be closest to the equilibrium value near their rims. Fe-Mg exchange
295 thermobarometry (given T, P, X_{grs} and molar Fe/Mg in clinopyroxene and garnet)
296 applied to a core-rim transect in a zoned garnet from experiment 8-GLOSS (an
297 experiment with large and relatively unzoned clinopyroxene) using the (Ellis and
298 Green 1979) calibration demonstrate a rim-ward approach toward the expected
299 equilibrium value (Fig. 5). This observation validates the analytical approach of
300 measuring mineral compositions near their rims.

301 In all of the experiments that were seeded with garnet (with the exception of
302 9-GLOSS), the garnet seeds have sharp edges and appear fragmented, suggesting no
303 dissolution of the seeds prior to crystallization. However, in the experiment 9-
304 GLOSS the garnet seed is rounded with irregular faces, suggesting at least a minimal
305 amount of dissolution prior to epitaxial crystallization of new garnet. Because the
306 Gore Mountain seed garnet is relatively Fe- and Mg-rich, this likely changed (at least
307 locally) the melt composition from which the garnets were crystallizing. In return,
308 this created new garnet growth that is relatively Fe and Mg rich (relative to 4-

309 GLOSS), and subsequently deficient in Ti relative to garnets from 4-GLOSS that were
310 grown without a seed.

311 Similarly, garnet-clinopyroxene Fe-Mg partition coefficients $K_{D1} =$
312 $(Fe/Mg)_{gt} / Fe/Mg_{cpx}$ for the experiments of Rapp and Watson 1995 and this study
313 match the experimental calibrations (Råheim and Green 1974; Ellis and Green 1979;
314 Pattison and Newton 1989; Ragna 2000) for Fe-Mg exchange. The spread in
315 calculated temperatures for this study (Fig. 6) are similar to the spread in higher-
316 temperature experiments of Rapp and Watson 1995— validation that even the
317 lower temperature garnets of this study approached equilibrium conditions.

318 **Substitution mechanisms**

319 Proyer et al., 2012 laid a theoretical framework for understanding possible
320 substitution mechanisms of octahedral Ti incorporation into garnet. These include:

- 321 (1) $^{VI}Ti^{4+} + ^{VIII}Na^{+} \leftrightarrow ^{VIII}M^{2+} + ^{VI}Al^{3+}$,
322 (2) $^{VI}Ti^{4+} + ^{VI}M^{2+} \leftrightarrow 2^{VI}Al^{3+}$,
323 (3) $^{VI}Ti^{4+} + ^{IV}Al^{3+} \leftrightarrow ^{VI}Al^{3+} + ^{IV}Si^{4+}$ (Ti—tschermak),
324 (4) $^{VI}Ti^{4+} + ^{IV}Fe^{3+} \leftrightarrow ^{VI}(Al,Fe)^{3+} + ^{IV}Si^{4+}$ (Ti-andradite),
325 (5) $^{VIII}\square + 2^{VI}Ti^{4+} \leftrightarrow ^{VIII}M^{2+} + 2^{VI}Al^{3+}$ (\square denotes vacancy).

326 Additionally, Ti incorporation into garnet could take place via direct substitution for
327 Si on the tetrahedral site:

- 328 (6) $^{IV}Ti^{4+} \leftrightarrow ^{IV}Si^{4+}$.

329 Incorporation of $^{VI}Ti^{4+}$ with $^{VIII}Na^{+}$ (mechanism 1) onto the dodecahedral site is a
330 plausible substitution mechanism in some natural systems where the measured Na

331 content of the garnet equals (Auzanneau et al. 2009) or exceeds Ti content (e.g. grt2
332 from (Krenn et al. 2008; Proyer et al. 2013). However, the concentration of Na in
333 many natural garnets is appreciably lower than that of Ti. In the experimental
334 garnets grown for this study, Na concentrations were near or below the EPMA
335 detection limit and far below the Ti content, reducing the possibility of the Na
336 substitution as a dominant substitution mechanism.

337 The roles of substitution mechanisms 2, 3 and 5 can be assessed by comparing
338 the Ti content of garnet with cation-normalized deficits on the Al and Si sites. If Ti
339 sits on the octahedral site via a coupled substitution with an octahedrally-
340 coordinated M^{2+} cation, the slope between Ti content and Al deficit on the Al site [2-
341 Al (a.p.f.u)] should equal 2. If the Ti-tschermak substitution dominates, there is no
342 net loss of Al with Ti incorporation, so the slope between Ti and Al deficit will equal
343 zero. Similar arguments can be made in Ti versus Si deficit space [3-Si (a.p.f.u)]. If
344 the Ti + M^{2+} substitution or vacancy mechanism dominate, the slope between Ti and
345 Si deficit should be zero, while the Ti-tschermak substitution mechanism will result
346 in a slope of 1.

347 Least-squares linear regression of the data in Ti versus Al deficit space (Fig. 7a)
348 exhibits a slope of 1.32— between the expected trends of mechanisms 2 and 3.
349 While closer in slope to the expected slope (2) for mechanism 2/5, the data are
350 shifted to a lower Al-deficit value. This would be expected if Al is also incorporated
351 onto the tetrahedral site (mechanism 3).

352 As in the case of the Ti vs. Al deficit trends, the slope of the data in Ti versus Si
353 deficit space (0.39) lies between mechanisms 2 or 5 and 3 (Fig. 7b). These combined

354 observations suggest Ti incorporation occurs predominately via both mechanisms 2
355 and 3. Integrating mechanisms 2 and 3 onto a single plot [Al deficit + 2(Si deficit)]
356 (Fig. 7c) yields a positive correlation with a slope of 2.07 ± 0.16 , within error of the
357 theoretical value. In Ti and Al-deficit or Si-deficit space, scatter from the linear
358 regression is likely a function of both the inherent analytical scatter and varying
359 contributions of the two substitution mechanisms to the individual experiments.

360 It is not possible to deconvolve the vacancy mechanism (mechanism 5) from
361 mechanism 2 in Ti versus Al deficit space, or from mechanism 3 in Ti versus Si
362 deficit space. However, the vacancy mechanism alone does not account for the
363 positive correlation between Ti and Si-deficit. Similarly, the andradite-type
364 substitution mechanism (mechanism 4) should result in positive trends between Ti
365 an Al-deficit and Si-deficit space, but alone cannot account for the total variability
366 observed in Figure 7. Whereas the combination of mechanisms 2 and 3 provide the
367 best fit to the data, mechanisms 4 and 5 could also contribute to the incorporation of
368 Ti into garnet. Using Al-deficit and Si-deficit calculations, it is clear that no one
369 substitution mechanism controls Ti incorporation in garnet.

370 If only the vacancy substitution (m5) is invoked, it fails to account for the
371 observed trend between Ti and Si-deficit, and convolving m5 with m3 to account for
372 the Ti vs. Si-deficit trend would push the slope in Ti versus Al-deficit space to a value
373 <1 , not >1 as demonstrated in Figure 7. The Fe^{3+} Ti-andradite mechanism (m4)
374 could conceivably account for the positive slope in Ti versus Si-deficit space, and the
375 substitution of Fe^{3+} for Al^{3+} in the octahedral site irrespective of Ti content could
376 occlude the use of Ti versus Al-deficit. Still, the slope <1 in Ti versus Si-deficit

377 suggests that m4 is not the only possible substitution mechanism responsible for Ti
378 incorporation.

379 In addition to the substitution mechanisms discussed above, Ti^{3+} could
380 substitute onto the octahedral site via a direct substitution for Al^{3+} (Krawczynski et
381 al., 2009), or Ti^{4+} could substitute for Si^{4+} on the tetrahedral site. For the sake of
382 brevity, these substitutions will be regarded as negligible contributions to the Ti
383 content of the experimental garnets and are not discussed further here (but see the
384 companion paper on XANES spectroscopy of natural garnets).

385 **Relationship between Ti and other cations in garnet**

386 Coupled substitution of Ti via mechanism 2 involves the incorporation of an
387 additional cation (Fe, Mg, Ca, or Mn) on the octahedral site in garnet. Trends
388 between Ti and the divalent cations can indicate which cations are most likely to be
389 involved in this mechanism. Still, because the dodecahedral site holds multiple
390 elements, chemical trends alone cannot directly discern which elements are being
391 incorporated octahedrally with Ti. Octahedral Mg has been observed in high
392 pressure systems (10s of GPa) as a component of majoritic garnet (Hazen et al.
393 1994) and more recently in the end-member garnet menzerite (Grew et al. 2010)
394 from granulite-facies rocks. Octahedral Fe^{2+} (in conjunction with octahedral Ti) is
395 suggested in the hypothetical end-member garnet morimotoite (Henmi et al. 1995)
396 while the large ionic radius of Ca is typically believed to inhibit octahedral Ca
397 solubility (Novak and Gibbs 1971; Bosenick et al. 2000).

398 Of the divalent cations, only Ca is positively correlated with Ti incorporation
399 over the entire experimental range (Fig. 8). This trend suggests that Ca content

400 plays a significant role in Ti incorporation. The large ionic radius of Ca imparts high
401 strain on the dodecahedral site (Armbruster and Geiger 1993; Ballaran et al. 1999),
402 and has also been shown to influence the bonding environment of the octahedral
403 and tetrahedral crystallographic sites. It also makes Ca substitution onto the
404 octahedral site unlikely (Bosenick et al. 2000). Additionally, the dodecahedral site in
405 high-Ti natural garnets [morimotoite ($\text{Ca}_3\text{TiFe}^{2+}\text{Si}_3\text{O}_{12}$) and schorlomite
406 ($\text{Ca}_3\text{Ti}_2\text{SiFe}_2^{3+}\text{O}_{12}$), (Grew et al. 2013)] is almost entirely occupied by Ca (Kuhberger
407 et al. 1989; Henmi et al. 1995; Chakhmouradian and McCammon 2005). Ultimately,
408 the covariance between Ti and Ca suggests that— regardless of the substitution
409 mechanism— increasing dodecahedral Ca results in an increase in octahedral Ti
410 solubility.

411 Unlike Ca, Mg decreases in concentration with increasing Ti (Fig. 8d). This
412 negative correlation does not immediately discount the possibility of $^{\text{VI}}\text{Mg}$ solubility
413 as a charge-balancing cation with $^{\text{VI}}\text{Ti}$, especially considering that its VI-fold ionic
414 radius is the closest of the divalent cations to $^{\text{VI}}\text{Al}^{3+}$. However, the range of run
415 conditions between experiments, differences in bulk compositions, varying degrees
416 of melting of multiple bulk compositions, multiple mineral assemblages could all
417 account for changes in Mg content irrespective of Ti.

418 There is no significant correlation between Ti and Mn in the experimental
419 garnets, yet the possibility that Mn is incorporated with Ti octahedrally cannot be
420 discounted. From an ionic radius perspective, Mn is less likely to incorporate with Ti
421 than Fe and the general increase in Fe with Ti suggests it is the most likely cation to
422 substitute octahedrally with Ti. However, many garnets from this study exhibit

423 higher Fe and lower Mg relative to other phase equilibrium studies (Fig. 8) and have
424 a negative trend in Fe versus Ti space compared to the positive trend exhibited in
425 other experimental studies. This trend can be explained by the convolution of
426 temperature and grossular content ultimately influencing Fe-Mg partitioning in
427 garnet. The effect of T and X_{grs} on Fe-Mg exchange between garnet and cpx has
428 been well-documented experimentally (Ellis and Green 1979; Pattison and Newton
429 1989). Decreasing T and increasing X_{grs} result in an increase in the garnet-cpx Fe-
430 Mg K_{D1} , where $K_{D1} = \frac{(Fe/Mg)_{gt}}{(Fe/Mg)_{cpx}}$. Compared to the experiments of
431 Rapp and Watson (1995), our experiments were performed at lower temperatures
432 and the garnets contain higher X_{grs} . These will produce a higher K_D and lead to
433 more Fe in the garnets. Despite the negative trend in Fe-Ti space exhibited by many
434 garnets in this study, the overall Fe content of garnets along the negative trend is
435 higher than the Fe content of garnets along the positive trend (Fig. 8c). The higher
436 Fe content of these garnets suggests the negative trend does not preclude Fe
437 incorporation on the octahedral site with Ti.

438 The discrepancy between Fe and Mg content relative to Ti from many of the
439 experiments of this study relative to other studies (Fig. 8c,d) is reflected in the
440 partitioning of Fe and Mg between garnet and melt and clinopyroxene (Fig. 9). Relative
441 to the Ti and grossular content of garnets, several experiments from this study have
442 elevated Fe/Mg values compared to those of Rapp and Watson 1995 (Fig. 9c,e). The
443 higher Fe/Mg fractions of these garnets is accompanied by higher Fe/Mg values in both
444 the clinopyroxene and melt (Fig. 9a,b). This apparent increase in Fe/Mg fractions of the

445 major phases in the experiments has no apparent affect on Ti concentration in the garnet,
446 which could indicate that Ca content and/or T have a greater influence on Ti
447 concentration than do the almandine or pyrope component of garnet.

448 The elevated Fe in some of the experimental garnets from this study relative to the
449 main body of data in Fig. 7c is not easily resolved by differences in phase assemblage, as
450 the phase assemblage is identical to many of the experiments on the main trend. Also,
451 experiments from all three bulk compositions are in both the high- and low-Fe groups,
452 suggesting bulk chemistry does not play a significant role in creating the elevated Fe
453 garnets.

454 A third possible explanation would be elevated Fe due to the presence of Fe³⁺ as
455 andradite (Ca₃Fe³⁺₂Si₃O₁₂). This is unlikely for several reasons. First, all experiments
456 reported in this study were buffered at the FMQ buffer, lower than the nickel-nickel
457 oxide buffer of the other studies reported in Figure 8 and therefore likely to contain less
458 Fe³⁺. Second, the increase in Fe is accompanied by a decrease in Mg (Fig. 7c,d).
459 Including ferric iron as andradite onto the octahedral site should not affect the solubility
460 of Mg on either the dodecahedral or octahedral sites.

461 Comparing the Ti content of garnet with Fe/Mg partitioning between garnet and
462 clinopyroxene reveals the most likely explanation for the observed trends. The Fe-rich
463 garnets are accompanied by Fe-rich clinopyroxene and melt, resulting in continuous
464 trends in TiO₂-K_{D1} space. The increase in Fe/Mg in garnet, clinopyroxene and melt could
465 reflect differences in bulk Fe or Fe activity of the melt, Fe loss in other studies, Fe
466 contamination from the sample preparation process, or uncharacterized phenomena.

467 **Factors controlling Ti incorporation**

468 Given the non-ideality of garnet solid solutions (Ellis and Green 1979; Harley
469 1984; Koziol and Bohlen 1992, 1992; Ungaretti et al. 1995; Nakamura 2009), the
470 size of analytical errors, and a lack of activity buffering phases (quartz,
471 aluminosilicate, rutile) in many experiments it has not been possible to fit a
472 thermodynamic partitioning model to garnet-melt partitioning behavior. Attempts
473 to create other Ti-based thermobarometers— e.g., for micas, where Ti incorporation
474 occurs through only the mechanism ${}^{\text{VI}}\text{Ti}^{4+} + {}^{\text{IV}}\text{Al}^{3+} \rightleftharpoons {}^{\text{VI}}\text{Al}^{3+} + {}^{\text{IV}}\text{Si}^{4+}$ — have yielded
475 mixed results. Auzanneau et al. (2009) demonstrated a positive pressure
476 dependence of Ti incorporation in experimentally-grown micas, and subsequently
477 calibrated a Ti-in-phengite barometer, while Chambers and Kohn (2012) observed
478 virtually no pressure dependence of Ti incorporation in a database of experimental
479 micas. Chambers and Kohn (2012) also note that the dependence of Ti-in-mica on
480 the compositions of the mineral phases involved in the reaction significantly
481 diminishes the application of Ti-in-mica for estimating T and P. In contrast, Henry et
482 al. (2005) created an empirical Ti-in-biotite geothermometer by fitting Ti to
483 $\text{Fe}/(\text{Fe}+\text{Mg})$ and T in a suite of peraluminous metapelites from Maine. In the
484 experimental garnets of this study, there is no obvious relationship solely between
485 Ti and T or Ti and P (Fig. 10).

486 Given the thermodynamic limitations stated above, we created an empirical
487 fit to the experimental data set using T, P, and various compositional parameters
488 [X_{grs} , $\text{Fe}/(\text{Fe}+\text{Mg})$ in garnet, melt composition (FM, M, and ASI parameters)].
489 Convolving garnet-melt partitioning, melt composition and temperature provided
490 the best empirical fit to the data.

491 Previous studies have demonstrated the systematic behavior of mineral-melt
492 K_{D2} values ($K_{D2} = \frac{X_{Ti}^{Gt}}{X_{Ti}^L}$, where X_{Ti}^{Gt} and X_{Ti}^L are the cation mol fractions of Ti in garnet
493 and coexisting silicate melt, respectively) with respect to T, P, $X_{H_2O}^L$, and melt
494 composition (Mahood and Hildreth 1983; Blundy and Wood 1994). Several melt
495 composition parameters were tested to obtain the best fit between melt
496 composition and K_D , including M (Watson and Harrison 1983; Boehnke et al. 2013),
497 ASI (Zen 1986) and the closely related FM (Ryerson and Watson 1987; Hayden and
498 Watson 2007), which was modified from the original M of Watson and Harrison
499 (1983) by inclusion of Mg and Fe $\left[FM = \frac{1}{Si} \cdot \frac{Na+K+2(Ca+Mg+Fe)}{Al} \right]$, where the element
500 symbols represent cation fractions). Both FM and its predecessor M are empirical,
501 quasi-thermodynamic melt composition parameters that capture the expected
502 inverse dependence of the activities of highly-charged ions (Zr^{4+} , Ti^{4+}) in the melt
503 upon melt SiO_2 content, as well as the role of univalent and divalent cations present
504 in the melt in excess of Al. (Watson 1976; Ryerson and Hess 1978; Dickinson Jr. and
505 Hess 1985; Ryerson and Watson 1987; Hayden and Watson 2007). As a predictor of
506 Ti uptake of garnet in equilibrium with felsic melt, FM yielded a better fit to our
507 data.

508 Garnet-melt K_{D2} values fit to $1/T$ (in Kelvin) and FM using a non-weighted
509 multiple linear regression yields the relationship:

$$510 \quad \ln K_{D2} = -1.701(\pm 0.984) + \frac{4358.18(\pm 1129.77)}{T} - 0.720(\pm 0.068)FM$$

511 with an adjusted $R^2=0.85$ (Fig. 12). The errors reported are errors in the fit of model
512 to the data, and do not take into account analytical uncertainties or the standard

513 errors of the measurements of individual garnets from a single experiment. Several
514 linear and non-linear curve fitting techniques were applied to the data, but
515 ultimately the multiple-linear regression yielded the best fit. Fitting of Ti between
516 garnet compositional parameters (Fe/Mg, X_{grs}), T and P without melt compositional
517 parameters yielded poor fits (adjusted R^2 values less than 0.3), suggesting a strong
518 melt composition effect on Ti incorporation.

519 This model relates a decrease in both temperature and FM value to an
520 increase in K_{D2} (Fig. 12), which is consistent with previous studies of Ti
521 mineral/melt equilibria (Ryerson and Watson 1987; Hayden and Watson 2007) and
522 is able to reliably estimate Ti content in garnet (Fig. 13). Over the experimental
523 range FM exerts stronger influence on partitioning than does T, as demonstrated by
524 the shallow slope of the FM isopleths in T- $\ln K_D$ space.

525 Unlike similar models that include a pressure term (Ryerson and Watson
526 1987), pressure was not included into this model as it resulted in a decrease in the
527 adjusted R^2 value of the linear regression fit and fitting errors on the coefficient of
528 the pressure term were larger than the coefficient itself. This does not discount the
529 possibility that pressure may influence the K_D , but rather that its effect is not
530 resolvable in this data set. Although there is no significant correlation between Ti
531 content of garnet and P over the investigated experimental range, at higher
532 pressures (5-15 GPa) Zhang et al., 2003 noticed an increase in Ti solubility
533 attributed to a significant majorite component (${}^VI\text{Si}^{4+} + {}^VI\text{Mg}^{2+} = 2{}^VI\text{Al}^{3+}$) in the
534 garnet. Increased partitioning of Ti into garnet due to an increase in the majorite
535 component is reasonable for mantle garnet, but this occurs at pressures much

536 higher than those experienced by most continental high-grade garnets, including
537 those containing exsolved rutile needles (Ague et al. 2013; Proyer et al. 2013; Zhang
538 et al. 2005a).

539 One of the interesting features of this model fit is the shift in Ti compatibility
540 between garnet and melt. As temperature and FM value decrease K_D reaches a point
541 ($\ln K_D > 0$) where Ti is more compatible in garnet than the melt. Low degree partial
542 melts of experimental intermediate to mafic rocks have melt FM values (and lower
543 T) that generate garnets into which Ti is compatible. Increasing temperature leads
544 to an increase in the degree of partial melting and ultimately the generation of
545 garnets that contain less Ti than the melt. There is significant scatter in the data
546 relative to the fit (Fig. 11) that reduces the utility of this model to understanding the
547 composition of garnet-bearing melts. Given the thermodynamic implications of a
548 shift in Ti compatibility between garnet and melt, the observations and the model fit
549 to garnet-melt Ti partitioning warrants future study. It should also be noted that—
550 relative to changes in Ti content of garnets— variations in the Ti content of the melt
551 play a strong role in the partitioning behavior of Ti between garnets and melt.

552 In natural systems, melting of metapelitic and metabasaltic rocks will initially
553 create leucosome melts in which Ti is incompatible relative to garnets that may
554 crystallize from the melt. For example, the melting of granulite-facies metapelites in
555 the Limpopo Belt of South Africa (Taylor et al. 2014) occurs via dehydration of
556 biotite and muscovite for garnet ± cordierite and orthopyroxene. Bulk “stromatic”
557 leucosomes from these metapelites have an FM value near 1, suggesting that garnet
558 crystallization will initially cause Ti depletion in the melt.

559 **Disparity between experimental and natural garnets**

560 Observations from natural high-grade systems support the conclusion from
561 our experiments that Ti and Mg are not positively correlated, which suggests that Ti
562 incorporation via mechanism 2 does not utilize Mg. Experimental results shown
563 here demonstrate that garnet can incorporate Ti up to several wt. % in garnets with
564 higher almandine and grossular components. High-grade natural garnets with
565 appreciable almandine and grossular components (e.g. UHT garnets of (Ague et al.
566 2013)) have Ti content up to 0.374 wt. %, and evidence of higher Ti solubility exists
567 in the form of crystallographically-aligned rutile needles. Contrastingly, the coesite-
568 bearing, grossular-poor Dora Maira pyrope (grown in the presence of rutile) has
569 almost no detectable Ti and no evidence of Ti loss through re-equilibration (Schertl
570 et al. 1991). Whereas it is difficult to include Ca onto the octahedral site in garnet,
571 the apparent increase in Ti solubility with increases in grossular and almandine
572 components in synthetic garnets should also be born out in observations from
573 natural systems (see Ackerson et al., this issue). Given the correlation between high
574 Ti in our experimental garnets and high Ca and Fe (up to 12.7 wt. % CaO) relative to
575 high grade pyrope-rich garnets that do not contain exsolved rutile needles, it is
576 likely that the solubility of Ti in natural pyrope-rich garnets is too low to
577 accommodate rutile exsolution. Furthermore, if Ca and/or Fe play significant roles
578 in the solubility of Ti in high-Ti garnets it is conceivable that the substitution
579 mechanisms governing Ti substitution (and Ti solubility) will change depending on
580 the grossular, almandine and/or andradite component of the garnets.

581 **Relevance to UHP/UHT systems and rutile exsolution**

582 The exsolution of crystallographically-aligned rutile needles in garnets from
583 high-grade metamorphic rocks is difficult to explain with closed-system reaction
584 mechanisms because Ti cannot be stoichiometrically removed from garnet.
585 Extensive discussion of the history of the rutile exsolution debate is available in the
586 literature (Van Roermund et al. 2000; Zhang et al. 2003; Hwang et al. 2007; Ague et
587 al. 2013; Proyer et al. 2013). Proyer et al. (2013) adopt open-system precipitation
588 (OSP) as a viable alternative to form rutile needles.

589 In OSP, garnet initially crystallizes with appreciable lattice-bound Ti. As the
590 garnet-bearing rock migrates through the crust, Ti solubility in the garnet decreases
591 and eventually reaches a point where rutile needles are exsolved from the garnet
592 lattice. In this model, Ti does not migrate out of the crystal, but rather nucleates
593 rutile needles in response to changing Ti solubility. OSP requires diffusive exchange
594 of atoms (O^{2-} , M^{2+} , Si^{4+} or e^-) between a static garnet-melt or garnet-matrix interface
595 and little to no movement of Ti out of the crystal. Another key requirement of OSP is
596 Al^{3+} solubility on the tetrahedral site and subsequent mobility to the octahedral site
597 during rutile exsolution. For example, (Proyer et al. 2013) suggest the following
598 reaction as one possible means to produce exsolved rutile:



599 In this example, oxygen and a divalent cation diffuse out of the crystal, Al moves to
600 the octahedral site and rutile is exsolved. Alternatively, the vacancy mechanism
601 (m5) could account for rutile exsolution, but would not require the long diffusive
602 length scales required to move divalent cations out of the garnet crystals.

603 OSP requires that garnets can incorporate enough Ti under reasonable
604 conditions to favor rutile exsolution upon exhumation, and substitution mechanisms
605 that can explain the seemingly non-stoichiometric exsolution of rutile from garnet.
606 Our experimental observations suggest that Ti can be incorporated at
607 concentrations greater than 2 wt % in garnet grown at UHP and UHT conditions,
608 and that Ti is incorporated by at least two substitution mechanisms in garnet.
609 Additionally, rutile exsolution from garnet requires exhumation rates slow enough
610 at and at high enough temperatures for Ti to diffuse through the garnet lattice to the
611 site of rutile nucleation. It is unclear whether or not the conditions needed to
612 exsolved rutile are conducive to loss of the charge-compensating M^{2+} cations out of
613 the garnet. Still, the theoretical framework of Proyer et al. (2013) and our
614 experimental demonstration of the possible substitution mechanisms governing Ti
615 incorporation into garnet provide a realistic picture of rutile exsolution from high-
616 grade metamorphic rocks.

617 **Implications**

618
619 Incorporation of Ti into experimentally-grown garnet is convolved with a
620 departure from ideal $M^{2+}:Al:Si$ stoichiometry. These stoichiometric departures can
621 be used to determine the mechanism(s) by which Ti is incorporated into the garnet
622 lattice. Ti incorporation in experimental garnets occurs on the octahedral site
623 primarily via two substitution mechanisms: ${}^VI Ti^{4+} + {}^VI M^{2+} \rightleftharpoons 2 {}^VI Al^{3+}$ and ${}^VI Ti^{4+} + {}^IV Al^{3+}$
624 $\rightleftharpoons {}^VI Al^{3+} + {}^IV Si^{4+}$. It is also conceivable that a vacancy or andradite-type mechanism
625 could contribute to Ti solubility in garnet, at least to a small degree. Although it is
626 not clear exactly which substitution mechanisms govern the majority of Ti solubility

627 in these garnets, it is important to note that no single substitution mechanisms can
628 account for the incorporation of Ti in garnet. This observation significantly
629 diminishes the possibility of thermodynamically-constrained Ti-in-garnet
630 thermobarometry. Additionally, the wide range of T, P, and compositions
631 investigated experimentally in this study allow for an empirical calibration of the Ti
632 content in garnet as a function of T and melt composition.

633 Our experimental results demonstrate that garnet grown experimentally at
634 eclogite and granulite facies conditions can incorporate up to 2.1 wt. % Ti, unlike
635 most mid-crustal garnets that typically contain less than 0.1 wt. % TiO₂. These
636 combined observations demonstrate that garnets from high-grade metamorphic
637 systems can incorporate Ti in sufficient quantities and via multiple substitution
638 mechanisms to facilitate exsolution of rutile needles. Garnets at the surface that
639 contain crystallographically-aligned exolved rutile needles probably experienced
640 high-grade metamorphic growth. In addition to Ti solubility considerations, garnets
641 would need to maintain elevated temperature for a sufficient amount of time to
642 allow for the diffusive movement of Ti through the lattice and subsequent rutile
643 exsolution. It is worth noting that the experiments of this study were performed at
644 relatively high temperatures and pressures and as such do not preclude Ti solubility
645 in lower-grade garnets.

646 As has been observed in high grade garnets (Ague and Eckert 2012; Axler
647 and Ague 2015), crystallographically-aligned rutile needles can be accompanied by
648 Ti depletion halos in the surrounding garnet. Future work to elucidate the
649 mechanisms and rates of Ti diffusion in garnet could be used to extract cooling and

650 exhumation rates of garnets containing exolved rutile needles (as described by
651 Cherniak et al. 2007 for quartz), especially if combined with a similar approach to P
652 depletion in garnets with exolved apatite needles (Axler and Ague 2015).

653 **Acknowledgments**

654
655 Many thanks are due to Thomas Mueller for editorial handling and Jay Ague
656 and Sumit Chakraborty for their reviews that improved the quality and content of
657 this manuscript. Thanks to Maureen Feineman and Cici Cruz-Urbe for discussion
658 during the development of this project, and to Jay Ague, Jen Axler, Jay Thomas and
659 Dustin Trail for discussion and critical comments throughout.

660

References Cited

- 661
662
663 Ague, J.J., and Eckert, J.O. (2012) Precipitation of rutile and ilmenite needles in garnet:
664 Implications for extreme metamorphic conditions in the Acadian Orogen, U.S.A.
665 American Mineralogist, 97, 840–855.
- 666 Ague, J.J., Eckert, J.O., Chu, X., Baxter, E.F., and Chamberlain, C.P. (2013) Discovery
667 of ultrahigh-temperature metamorphism in the Acadian orogen, Connecticut,
668 USA. *Geology*, 41, 271–274.
- 669 Alifirova, T.A., Pokhilenko, L.N., Ovchinnikov, Y.I., Donnelly, C.L., Riches, A.J.V., and
670 Taylor, L.A. (2012) Petrologic origin of exsolution textures in mantle minerals:
671 evidence in pyroxenitic xenoliths from Yakutia kimberlites. *International Geology*
672 *Review*, 54, 1071–1092.
- 673 Armbruster, T., and Geiger, C. (1993) Andradite crystal chemistry, dynamic X-site
674 disorder and structural strain in silicate garnets. *European Journal of Mineralogy*,
675 5, 59–72.
- 676 Auzanneau, E., Schmidt, M.W., Vielzeuf, D., and Connolly, J. a. D. (2009) Titanium in
677 phengite: a geobarometer for high temperature eclogites. *Contributions to*
678 *Mineralogy and Petrology*, 159, 1–24.
- 679 Axler, J.A., and Ague, J.J. (2015) Exsolution of Rutile or Apatite Precipitates
680 Surrounding Ruptured Inclusions in Garnet from UHT and UHP rocks. *Journal of*
681 *Metamorphic Geology*, n/a–n/a.
- 682 Ballaran, T.B., Carpenter, M.A., Geiger, C.A., and Koziol, A.M. (1999) Local structural
683 heterogeneity in garnet solid solutions. *Physics and Chemistry of Minerals*, 26,
684 554–569.
- 685 Bastin, G.F., van Loo, F.J.J., Vosters, P.J.C., and Vrolijk, J.W.G.A. (1984) An iterative
686 procedure for the correction of secondary fluorescence effects in electron-probe
687 microanalysis near phase boundaries. *Spectrochimica Acta*, 39B, 1517–1522.
- 688 Baxter, E.F., Ague, J.J., and Depaolo, D.J. (2002) Prograde temperature–time evolution
689 in the Barrovian type–locality constrained by Sm/Nd garnet ages from Glen
690 Clova, Scotland. *Journal of the Geological Society*, 159, 71–82.
- 691 Boehnke, P., Watson, E.B., Trail, D., Harrison, T.M., and Schmitt, A.K. (2013) Zircon
692 saturation re-revisited. *Chemical Geology*, 351, 324–334.
- 693 Bosenick, A., Dove, M.T., and Geiger, C.A. (2000) Simulation studies on the pyrope-
694 grossular garnet solid solution. *Physics and Chemistry of Minerals*, 27, 398–418.
- 695 Chakhmouradian, A.R., and McCammon, C.A. (2005) Schorlomite: a discussion of the
696 crystal chemistry, formula, and inter-species boundaries. *Physics and Chemistry*
697 *of Minerals*, 32, 277–289.

- 698 Chambers, J.A., and Kohn, M.J. (2012) Titanium in muscovite, biotite, and hornblende:
699 Modeling, thermometry, and rutile activities of metapelites and amphibolites.
700 American Mineralogist, 97, 543–555.
- 701 Cherniak, D.J., Watson, E.B., and Wark, D.A. (2007) Ti diffusion in quartz. Chemical
702 Geology, 236, 65–74.
- 703 Dickinson Jr., J.E., and Hess, P.C. (1985) Rutile solubility and titanium coordination in
704 silicate melts. *Geochimica et Cosmochimica Acta*, 49, 2289–2296.
- 705 Ellis, D.J., and Green, D.H. (1979) An experimental study of the effect of Ca upon
706 garnet-clinopyroxene Fe-Mg exchange equilibria. *Contributions to Mineralogy
707 and Petrology*, 71, 13–22.
- 708 Feenstra, A., and Engi, M. (1998) An experimental study of the Mg-Fe exchange between
709 garnet and ilmenite. *Contributions to Mineralogy and Petrology*, 131, 379–392.
- 710 Fournelle, J. (2007) Problems in Trace Element EPMA: Modeling Secondary
711 Fluorescence with PENEPMMA. AGU Fall Meeting Abstracts, 51, 0329.
- 712 Fournelle, J. (2007) The Problem of Secondary Fluorescence in EPMA in the Application
713 of the Ti-in-Zircon Geothermometer and the Utility of PENEPMMA Monte Carlo
714 Program. *Microscopy and Microanalysis*, 13, 1390–1391.
- 715 Grew, E.S., Marsh, J.H., Yates, M.G., Lazic, B., Armbruster, T., Locock, A., Bell, S.W.,
716 Dyar, M.D., Bernhardt, H.-J., and Medenbach, O. (2010) Menzerite-(Y), a new
717 species, $\{(Y,REE)(Ca,Fe^{2+})_2\}[(Mg,Fe^{2+})(Fe^{3+},Al)](Si_3)O_{12}$, from a felsin
718 granulite, Parry Sound, Ontario, and a new garnet end-member,
719 $\{Y_2Ca\}[Mg_2](Si_3)O_{12}$. *The Canadian Mineralogist*, 48, 1171–1193.
- 720 Grew, E.S., Locock, A.J., Mills, S.J., Galuskina, I.O., Galuskin, E.V., and Halenius, U.
721 (2013) Nomenclature of the garnet supergroup. *American Mineralogist*, 98, 785–
722 811.
- 723 Gwalani, L.G., Rock, N.M.S., Ramasamy, R., Griffin, B.J., and Mulai, B.P. (2000)
724 Complexely zoned Ti-rich melanite-schorlomite garnets from Ambadungar
725 carbonatite-alkalic complex, Deccan Igneous Province, Gujarat State, Western
726 India. *Journal of Asian Earth Sciences*, 18, 163–176.
- 727 Harley, S.L. (1984) An experimental study of the partitioning of Fe and Mg between
728 garnet and orthopyroxene. *Contributions to Mineralogy and Petrology*, 86, 359–
729 373.
- 730 Hayden, L.A., and Watson, E.B. (2007) Rutile saturation in hydrous siliceous melts and
731 its bearing on Ti-thermometry of quartz and zircon. *Earth and Planetary Science
732 Letters*, 258, 561–568.

- 733 Hazen, R., Downs, R., Finger, L., and Conrad, P. (1994) Crystal Chemistry of Ca-bearing
734 majorite. *American Mineralogist*, 79, 581–584.
- 735 Henmi, C., Kusachi, I., and Henmi, K. (1995) Morimotoite, $\text{Ca}_3\text{TiFe}_2\text{SiO}_{12}$, a new
736 titanian garnet from Fuka, Okayama Prefecture, Japan. *Mineralogical Magazine*,
737 59, 115–120.
- 738 Henry, D.J., Guidotti, C.V., and Thompson, J.A. (2005) The Ti-saturation surface for
739 low-to-medium pressure metapelitic biotites: Implications for geothermometry
740 and Ti-substitution mechanisms. *American Mineralogist*, 90, 316–328.
- 741 Huggins, F.E., Virgo, D., and Huckenholz, H.G. (1977) Titanium-containing silicate
742 garnets. II. The crystal chemistry of melanites and schorlomites. *American*
743 *Mineralogist*, 62, 646–665.
- 744 Hwang, S.L., Yui, T.F., Chu, H.T., Shen, P., Schertl, H.P., Zhang, R.Y., and Liou, J.G.
745 (2007) On the origin of oriented rutile needles in garnet from UHP eclogites.
746 *Journal of Metamorphic Geology*, 25, 349–362.
- 747 Jercinovic, M.J., Williams, M.L., and Lane, E.D. (2008) In-situ trace element analysis of
748 monazite and other fine-grained accessory minerals by EPMA. *Chemical*
749 *Geology*, 254, 197–215.
- 750 Kohn, M.J., and Spear, F.S. (1991a) Error propagation for barometers; 1, Accuracy and
751 precision of experimentally located end-member reactions. *American*
752 *Mineralogist*, 76, 128–137.
- 753 ——— (1991b) Error propagation for barometers; 2, Application to rocks. *American*
754 *Mineralogist*, 76, 138–147.
- 755 Koziol, A.M., and Bohlen, S.R. (1992) Solution properties of almandine-pyrope garnet as
756 determined by phase equilibrium experiments. *The American mineralogist*, 77,
757 765–773.
- 758 Krawczynski, M.J., Sutton, S.R., Grove, T.L., Newville, M. (mit), and (UofC) (2009)
759 Titanium oxidation state and coordination in the lunar high-titanium glass source
760 mantle. Advanced Photon Source (APS), Argonne National Laboratory (ANL),
761 Argonne, IL (US).
- 762 Krenn, K., Bauer, C., Proyer, A., Mposkos, E., and Hoinkes, G. (2008) Fluid entrapment
763 and reequilibration during subduction and exhumation: A case study from the
764 high-grade Nestos shear zone, Central Rhodope, Greece. *Lithos*, 104, 33–53.
- 765 Krogh, E.J. (1988) The garnet-clinopyroxene Fe-Mg geothermometer — a
766 reinterpretation of existing experimental data. *Contributions to Mineralogy and*
767 *Petrology*, 99, 44–48.

- 768 Kuhberger, A., Fehr, T., Huckenholz, H.G., and Amthauer, G. (1989) Crystal Chemistry
769 of a Natural Schorlomite and Ti-Andradites Synthesized at Different Oxygen
770 Fugacities. *Physics and Chemistry of Minerals*, 16, 734–740.
- 771 Lanzirotti, A. (1995) Yttrium zoning in metamorphic garnets. *Geochimica et*
772 *Cosmochimica Acta*, 59, 4105–4110.
- 773 Nakamura, D. (2009) A new formulation of garnet–clinopyroxene geothermometer based
774 on accumulation and statistical analysis of a large experimental data set. *Journal*
775 *of Metamorphic Geology*, 27, 495–508.
- 776 Novak, G.A., and Gibbs, G.V. (1971) The crystal chemistry of the silicate garnets.
777 *American Mineralogist*, 56, 791–825.
- 778 Pattison, D.R.M., and Newton, R.C. (1989) Reversed experimental calibration of the
779 garnet-clinopyroxene Fe — Mg exchange thermometer. *Contributions to*
780 *Mineralogy and Petrology*, 101, 87–103.
- 781 Plank, T., and Langmuir, C.H. (1998) The chemical composition of subducting sediment
782 and its consequences for the crust and mantle. *Chemical Geology*, 145, 325–394.
- 783 Proyer, A., Habler, G., Abart, R., Wirth, R., Krenn, K., and Hoinkes, G. (2013) TiO₂
784 exsolution from garnet by open-system precipitation: evidence from
785 crystallographic and shape preferred orientation of rutile inclusions. *Contributions*
786 *to Mineralogy and Petrology*, 166, 211–234.
- 787 Pyle, J.M., and Spear, F.S. (2003) Four generations of accessory-phase growth in low-
788 pressure migmatites from SW New Hampshire. *American Mineralogist*, 88, 338–
789 351.
- 790 Qian, Q., and Hermann, J. (2013) Partial melting of lower crust at 10–15 kbar: constraints
791 on adakite and TTG formation. *Contributions to Mineralogy and Petrology*, 165,
792 1195–1224.
- 793 Råheim, A., and Green, D.H. (1974) Experimental determination of the temperature and
794 pressure dependence of the Fe-Mg partition coefficient for coexisting garnet and
795 clinopyroxene. *Contributions to Mineralogy and Petrology*, 48, 179–203.
- 796 Rapp, R.P., and Watson, E.B. (1995) Dehydration Melting of Metabasalt at 8–32 kbar:
797 Implications for Continental Growth and Crust-Mantle Recycling. *Journal of*
798 *Petrology*, 36, 891–931.
- 799 Ravna, K. (2000) The garnet–clinopyroxene Fe²⁺–Mg geothermometer: an updated
800 calibration. *Journal of Metamorphic Geology*, 18, 211–219.
- 801 Richter, F.M., Davis, A.M., DePaolo, D.J., and Watson, E.B. (2003) Isotope fractionation
802 by chemical diffusion between molten basalt and rhyolite. *Geochimica et*
803 *Cosmochimica Acta*, 67, 3905–3923.

- 804 Ryerson, F.J., and Hess, P.C. (1978) Implications of liquid-liquid distribution coefficients
805 to mineral-liquid partitioning. *Geochimica et Cosmochimica Acta*, 42, 921–932.
- 806 Ryerson, F.J., and Watson, E.B. (1987) Rutile saturation in magmas: implications for
807 TiNbTa depletion in island-arc basalts. *Earth and Planetary Science Letters*, 86,
808 225–239.
- 809 Schertl, H.-P., Schreyer, W., and Chopin, C. (1991) The pyrope-coesite rocks and their
810 country rocks at Parigi, Dora Maira Massif, Western Alps: detailed petrography,
811 mineral chemistry and PT-path. *Contributions to Mineralogy and Petrology*, 108,
812 1–21.
- 813 Scordari, F., Schingaro, E., Malitesta, C., and Pedrazzi, G. (2003) Crystal chemistry of
814 Ti-bearing garnets with volcanic origin p. 5605. Presented at the EGS - AGU -
815 EUG Joint Assembly.
- 816 Tailby, N.D. (2009) New experimental techniques for studying: (i) trace element
817 substitution in minerals, and (ii) determining S-L-V relationships in silicate-H₂O
818 systems at high pressure. Australian National University.
- 819 Taylor, J., Nicoli, G., Stevens, G., Frei, D., and Moyen, J.-F. (2014) The processes that
820 control leucosome compositions in metasedimentary granulites: perspectives from
821 the Southern Marginal Zone migmatites, Limpopo Belt, South Africa. *Journal of*
822 *Metamorphic Geology*, 32, 713–742.
- 823 Thöni, M. (2002) Sm–Nd isotope systematics in garnet from different lithologies (Eastern
824 Alps): age results, and an evaluation of potential problems for garnet Sm–Nd
825 chronometry. *Chemical Geology*, 185, 255–281.
- 826 Ungaretti, L., Leona, M., Merli, M., and Oberti, R. (1995) Non-ideal solid-solution in
827 garnet: crystal-structure evidence and modelling. *European Journal of*
828 *Mineralogy*, 7, 1299–1312.
- 829 Van Roermund, H.L.M., Drury, M.R., Barnhoorn, A., and De Ronde, A. (2000) Non-
830 silicate inclusions in garnet from an ultra-deep orogenic peridotite. *Geological*
831 *Journal*, 35, 209–229.
- 832 Wark, D.A., and Watson, E.B. (2006) TitaniQ: a titanium-in-quartz geothermometer.
833 *Contributions to Mineralogy and Petrology*, 152, 743–754.
- 834 Watson, E.B. (1976) Two-liquid partition coefficients: Experimental data and
835 geochemical implications. *Contributions to Mineralogy and Petrology*, 56, 119–
836 134.
- 837 Watson, E.B., and Harrison, T.M. (1983) Zircon saturation revisited: temperature and
838 composition effects in a variety of crustal magma types. *Earth and Planetary*
839 *Science Letters*, 64, 295–304.

- 840 Waychunas, G.A. (1987) Synchrotron radiation XANES spectroscopy of Ti in minerals:
841 Effects of Ti bonding distances, Ti valence, and site geometry on absorption edge
842 structure. *American Mineralogist*, 72, 89–101.
- 843 Wentorf, R.H. (1956) The formation of Gore Mountain [New York] garnet and
844 hornblende at high temperature and pressure. *American Journal of Science*, 254,
845 413–419.
- 846 Ye, K., Cong, B., and Ye, D. (2000) The possible subduction of continental material to
847 depths greater than 200 km. *Nature*, 407, 734–736.
- 848 Yoder, H.S., and Tilley, C.E. (1962) Origin of Basalt Magmas: An Experimental Study of
849 Natural and Synthetic Rock Systems. *Journal of Petrology*, 3, 342–532.
- 850 Zen, E.-A. (1986) Aluminum Enrichment in Silicate Melts by Fractional Crystallization:
851 Some Mineralogic and Petrographic Constraints. *Journal of Petrology*, 27, 1095–
852 1117.
- 853 Zhang, R.Y., Zhai, S.M., Fei, Y.W., and Liou, J.G. (2003) Titanium solubility in
854 coexisting garnet and clinopyroxene at very high pressure: the significance of
855 exsolved rutile in garnet. *Earth and Planetary Science Letters*, 216, 591–601.
- 856 Zhang, R.Y., Liou, J.G., Zheng, J.-P., Griffin, W.L., Yui, T.-F., and O'Reilly, S.Y. (2005)
857 Petrogenesis of the Yangkou layered garnet-peridotite complex, Sulu UHP
858 terrane, China. *American Mineralogist*, 90, 801–813.

859 **List of Figure Captions**

- 860
- 861 **Figure 1:** Typical experimental assembly design for fO_2 -buffered piston cylinder
862 experiment.
- 863 **Figure 2:** Temperature and pressure range of experiments. Black circles are
864 experiments from this study, open squares from Qian and Hermann (2013), black
865 plus symbols from Rapp et al. (1995), and open circles are from Tailby (2009).
866 Metamorphic facies adapted from Spear et al., 1993. Geobarometric gradient
867 calculated assuming an average crustal thickness of 41.1 km and an average crustal
868 density of 2830 kg/m³ from Christiansen and Mooney. Geotherm with pressure
869 from Sclater et al., 1980.

870 **Figure 3:** Secondary fluorescence in garnet adjacent to ilmenite. The garnet-
871 ilmenite sandwich experiment and PENEPM simulation demonstrate significant
872 secondary fluorescence at distances up to 45 μm from the garnet-ilmenite interface.
873 In an experimental garnet with an ilmenite inclusion, secondary fluorescence is not
874 observed until 5 μm from the interface.

875 **Figure 4:** Results of garnet synthesis experiments. **a** Typical $f\text{O}_2$ -buffered run
876 product with the experiment and $f\text{O}_2$ buffer juxtaposed against one another with a
877 Pd foil membrane to facilitate H movement between capsules, the charges and
878 subsequent $f\text{O}_2$ buffering at FMQ. **b** Backscatter electron images (BSE) of several
879 experimental run products. In some experiments (e.g. GLOSS at 850 $^\circ\text{C}$ and 1.5 GPa)
880 garnets are large and relatively inclusion free, and contain segregated melt pools
881 large enough for analysis. Conversely, other experiments (e.g. MORB at 850 $^\circ\text{C}$ and
882 2.5 GPa) contain garnets with too many Fe-Ti oxides to be analyzed without
883 secondary fluorescence contamination, and melt segregations too small to analyze.

884 **Figure 5:** Core-rim changes in Ti content and garnet-clinopyroxene Fe/Mg K_D in a
885 garnet from sample 8-GLOSS. The horizontal line is the K_D for this garnet
886 composition, temperature and pressure estimated using the garnet-clinopyroxene
887 Fe-Mg exchange thermobarometer from Ellis and Green, 1979. The rim-ward
888 approach of the K_D to the expected value suggests cores of zoned garnets are out of
889 chemical equilibrium with the melt and rims of other mineral phases.

890 **Figure 6:** Known experimental temperatures compared to temperatures calculated
891 using multiple models for Fe-Mg partitioning between garnet and clinopyroxene.
892 Black line is the 1:1 line between experimental and calculated temperatures.

893 Colored lines are linear regressions to the calculated temperature, corresponding in
894 color to the model fits. Colored dashed lines are the 95% confidence bands for the
895 linear regressions.

896 **Figure 7:** Relationships between Ti and oxide-normalized deficits in Al and Si.

897 Dashed lines represent the ideal vectors for substitution mechanisms 2, 3, and 5.

898 **a,b** Individually, Ti versus Al- and Si-deficits do not match the ideal vectors. **c**

899 Combining substitution mechanism 2 and 3 yields a reasonable fit to the idealized
900 substitution vectors.

901 **Figure 8:** Variations between Ti and M^{2+} cations in garnet, expressed in atoms per
902 formula unit (a.p.f.u.), based on 12 oxygens.

903 **Figure 9:** Relationship between Ti and Fe/Mg content of garnet and other phases.

904 Open circles are samples from this study that fall along the trend of the Rapp and

905 Watson 1995 data in figure 7c,d. **a,b** Molar Fe/Mg fractions in garnet compared to

906 molar Fe/Mg fractions in clinopyroxene and melt, demonstrating an overall increase

907 in Fe/Mg content of all three phases. **c,d** Grossular content of garnet versus Fe/Mg

908 fractions in garnet and Fe/Mg partitioning between garnet and clinopyroxene. Data

909 from Ellis and Green 1979 added to demonstrate the spread in data from a study

910 used to calibrate a garnet-clinopyroxene Fe-Mg partitioning thermobarometer. **e,f** Ti

911 content versus Fe/Mg fraction and garnet-clinopyroxene Fe-Mg exchange.

912 **Figure 10:** Ti versus T ($^{\circ}$ C) and P (GPa) in experimental garnets.

913 **Figure 11:** Model fit to garnet melt K_D values. **a** FM versus $\ln K_D$ contoured to T. **b** T

914 versus $\ln K_D$ for experiments whose melt compositions were within ± 0.05 of integer

915 FM values.

916 **Figure 12:** Three dimensional representation of the model fit between $\ln K_D$, $1/T$
917 and FM.

918 **Figure 13:** X_{Ti}^{Gt} (mole fraction Ti in garnet) observed from experiments versus the
919 values calculated using the empirical fit.

920

921
922

Tables

Table 1: Bulk compositions of starting materials

	GLOSS*	AMPH*	MORB
SiO ₂	66.17	53.11	49.43
TiO ₂	0.67	1.23	1.62
Al ₂ O ₃	13.48	17.22	15.97
Fe ₂ O ₃	—	—	2.02
FeO	6.04 [†]	11.72 [†]	7.61
MnO	0.38	0.23	0.17
MgO	2.81	6.82	8.5
CaO	5.07	4.3	10.73
Na ₂ O	2.82	4.51	2.87
K ₂ O	2.35	0.85	0.18
P ₂ O ₅	0.19	—	0.15
H ₂ O	—	—	0.12

*indicates synthetic starting material, [†]represents total Fe

923
924

Table 2: Phase assemblages from experiments

	T (°C)	P (Gpa)	assemblage*
10-GLOSS	800	1.5	grt, cpx, ilm, zrn, mlt
5-GLOSS	800	1.5	grt, cpx, opx, ilm, zrn, mlt
10-MORB	800	1.5	grt, cpx, amp, rt, zrn, spn, mlt
10-AMPH	800	1.5	grt, cpx, amp, ilm, zrn, mlt
5-AMPH	850	1.5	grt, cpx, amp, ilm, mag, zrn, mlt
8-GLOSS	850	1.5	grt, cpx, ilm, zrn, mlt
17-GLOSS	850	1.5	grt, cpx, ilm, zrn, mlt
17-AMPH	850	1.5	grt, cpx, opx, amp, ilm, zrn, mlt
4-GLOSS	900	1.5	grt, cpx, ilm, zrn, mlt
9-GLOSS	900	1.5	grt, cpx, ilm, zrn, mlt
4-MORB	900	1.5	grt, cpx, rt, zrn, spn, mlt
4-AMPH	900	1.5	grt, cpx, amp, ilm, zrn, mlt
7-AMPH	950	1.5	grt, ilm, zrn, mlt
15-GLOSS	800	2.5	grt, cpx, rt, qz, zrn, mlt
15-MORB	800	2.5	grt,cpx, rt, zrn, mlt
15-AMPH	800	2.5	grt, cpx, rt, zrn, mlt
13-GLOSS	850	2.5	grt, cpx, ilm, rt, zrn, mlt
12-MORB	850	2.5	grt, cpx, rt, zrn, mlt
11-AMPH	850	2.5	grt, cpx, opx, ilm, zrn, mlt
14-GLOSS	900	2.5	grt, cpx, ilm, rt, zrn, mlt
14-MORB	900	2.5	grt, cpx, rt, zrn, mlt
14-AMPH	900	2.5	grt, cpx, opx, ilm, zrn, mlt

*Abbreviations from Whitney and Evans, 2010. (grt) garnet, (cpx) clinopyroxene, (opx) orthopyroxene, (amp) amphibole, (ilm) ilmenite, (rt) rutile, (zrn) zircon, (spn) sphene/titanite, (mlt) melt

925
926

Table 3: Compositions of experimental garnets

	10-GLOSSb	10-GLOSS	5-GLOSS	10-MORB	10-AMPH					
T (°C)	800	800	800	800	800					
P (Gpa)	1.5	1.5	1.5	1.5	1.5					
time (hr)	24	48	72	48	48					
garnet seed*	Y	Y	Y	Y	Y					
no. analyses	12	37	15	14	12					
	<u>wt</u> <u>%**</u>	<u>O-</u> <u>nrml</u>	<u>wt %</u>	<u>O-</u> <u>nrml</u>						
Si***	37.01	2.95	36.43	2.94	36.73	2.97	38.59	2.95	36.98	2.94
SE	0.17	0.01	0.08	0.01	0.30	0.02	0.14	0.01	0.19	0.01
Ti	1.56	0.09	1.56	0.09	1.32	0.08	1.03	0.06	0.96	0.06
SE	0.03	0.00	0.02	0.00	0.09	0.00	0.06	0.00	0.23	0.01
Al	19.36	1.82	19.07	1.81	19.03	1.81	21.83	1.97	20.54	1.92
SE	0.31	0.03	0.26	0.02	0.16	0.02	0.14	0.01	0.32	0.03
Fe	27.60	1.84	27.68	1.87	25.77	1.74	20.83	1.33	31.00	2.06
SE	0.48	0.04	0.75	0.05	0.36	0.02	0.24	0.02	0.33	0.04
Mn	1.15	0.08	1.36	0.09	2.66	0.18	1.21	0.08	0.36	0.02
SE	0.15	0.01	0.06	0.02	0.03	0.00	0.08	0.01	0.04	0.00
Mg	1.66	0.20	1.92	0.23	2.73	0.33	5.63	0.64	3.79	0.45
SE	0.28	0.01	0.18	0.01	0.11	0.02	0.25	0.02	0.92	0.04
Ca	12.70	1.08	11.77	1.02	10.64	0.92	11.82	0.97	6.88	0.59
SE	0.58	0.05	0.52	0.06	0.27	0.02	0.21	0.02	0.57	0.03
SUM	101.05		99.79		98.87		100.95		100.52	
aldef		0.18		0.19		0.19		0.03		0.08
SE		0.03		0.02		0.02		0.01		0.03
Si def		0.05		0.06		0.03		0.05		0.06
SE		0.01		0.01		0.02		0.01		0.01
Al def + 2 Sdef		0.29		0.31		0.24		0.13		0.20
SE		0.01		0.01		0.01		0.01		0.02
ex cat		0.19		0.21		0.18		0.02		0.12
SE		0.07		0.08		0.04		0.04		0.07
X _{grs}		0.34		0.32		0.29		0.32		0.19
X _{alm}		0.58		0.58		0.55		0.44		0.66
X _{prp}		0.06		0.07		0.10		0.21		0.14
X _{sps}		0.02		0.03		0.06		0.03		0.01

927
928

Table 3 cont'd: Compositions of experimental garnets

	5-AMPH		8-GLOSS		17-GLOSS		17-AMPH		4-GLOSS	
T (°C)	800		850		850		850		900	
P (Gpa)	1.5		1.5		1.5		1.5		1.5	
time (hr)	72		48		48		48		48	
garnet seed*	Y		Y		Y		Y		N	
no. analyses	21		32		6		15		12	
	<u>wt %</u>	<u>Q-</u> <u>nrml</u>								
Si**	37.43	2.98	37.02	2.95	37.78	2.97	37.05	2.97	37.00	2.94
SD	0.22	0.02	0.34	0.03	0.51	0.04	0.19	0.02	0.10	0.01
Ti	0.91	0.05	1.44	0.09	1.67	0.10	1.34	0.08	1.89	0.11
SD	0.02	0.00	0.14	0.01	0.12	0.01	0.34	0.01	0.16	0.01
Al	20.11	1.89	19.74	1.85	20.04	1.85	19.78	1.87	19.56	1.83
SD	0.18	0.02	0.57	0.06	0.30	0.03	0.27	0.03	0.27	0.03
Fe	28.20	1.88	29.67	1.98	29.30	1.92	30.14	2.02	26.19	1.74
SD	0.35	0.02	0.75	0.05	0.51	0.04	0.46	0.04	1.95	0.13
Mn	0.94	0.06	1.32	0.09	1.65	0.11	0.41	0.03	2.13	0.14
SD	0.25	0.01	0.13	0.01	0.02	0.00	0.08	0.00	0.20	0.02
Mg	4.11	0.49	2.53	0.30	2.36	0.28	3.44	0.41	3.52	0.42
SD	0.41	0.04	0.26	0.04	0.62	0.04	0.18	0.02	0.27	0.03
Ca	7.90	0.67	9.15	0.78	9.29	0.78	7.55	0.65	9.88	0.84
SD	0.27	0.03	0.51	0.03	0.25	0.02	0.26	0.01	1.02	0.09
	99.60		100.88		102.09		99.71		100.17	
aldef		0.11		0.15		0.15		0.13		0.17
SE		0.02		0.06		0.03		0.03		0.03
Si def		0.02		0.05		0.03		0.03		0.06
SE		0.02		0.03		0.04		0.02		0.01
Al def + 2 Sdef		0.15		0.25		0.21		0.20		0.29
SE		0.01		0.03		0.02		0.01		0.01
ex cat		0.10		0.15		0.09		0.10		0.14
SE		0.05		0.08		0.06		0.05		0.16
X _{grs}		0.22		0.25		0.25		0.21		0.27
X _{alm}		0.61		0.63		0.62		0.65		0.55
X _{prp}		0.16		0.10		0.09		0.13		0.13
X _{sps}		0.02		0.03		0.04		0.01		0.05

929
930

Table 3 cont'd: Compositions of experimental garnets

	9-GLOSS		4-MORB		4-AMPH		7-AMPH		15-GLOSS	
T (°C)	900		900		900		950		800	
P (Gpa)	1.5		1.5		1.5		1.5		2.5	
time (hr)	48		48		48		48		48	
garnet seed*	Y		N		N		Y		Y	
no. analyses	14		13		16		15		10	
	<u>wt %</u>	<u>O- nrml</u>								
Si**	37.24	2.94	38.35	2.94	38.18	3.01	38.90	2.94	37.39	2.93
SD	0.26	0.02	0.25	0.02	0.22	0.02	0.22	0.02	0.49	0.04
Ti	0.39	0.02	1.62	0.09	1.15	0.07	2.04	0.12	1.63	0.10
SD	0.10	0.00	0.11	0.01	0.09	0.01	0.15	0.01	0.23	0.01
Al	21.58	2.01	21.39	1.93	19.54	1.81	20.95	1.87	20.71	1.92
SD	0.10	0.01	0.11	0.01	0.14	0.01	0.21	0.02	0.29	0.03
Fe	26.85	1.77	19.70	1.26	27.40	1.81	20.58	1.30	26.99	1.77
SD	0.37	0.02	0.25	0.01	0.32	0.02	0.44	0.02	0.52	0.04
Mn	1.85	0.12	0.88	0.06	0.63	0.04	0.78	0.05	0.67	0.04
SD	0.01	0.00	0.17	0.00	0.06	0.01	0.08	0.00	0.09	0.00
Mg	4.96	0.58	7.82	0.89	4.69	0.55	9.47	1.07	3.11	0.36
SD	0.07	0.01	0.11	0.03	0.06	0.01	0.06	0.03	0.37	0.04
Ca	6.92	0.58	9.97	0.82	8.64	0.73	8.24	0.67	10.52	0.88
SD	0.27	0.01	0.33	0.03	0.19	0.02	0.41	0.03	0.28	0.02
	99.79		99.72		100.23		100.95		101.02	
aldef		-0.01		0.07		0.19		0.13		0.08
SE		0.01		0.01		0.01		0.02		0.03
Si def		0.06		0.06		-0.01		0.06		0.07
SE		0.02		0.02		0.02		0.02		0.04
Al def + 2 Sdef		0.11		0.19		0.17		0.25		0.21
SE		0.01		0.01		0.01		0.01		0.02
ex cat		0.06		0.03		0.13		0.09		0.06
SE		0.03		0.04		0.03		0.04		0.06
X _{grs}		0.19		0.27		0.23		0.22		0.29
X _{alm}		0.58		0.42		0.58		0.42		0.58
X _{prp}		0.19		0.29		0.18		0.35		0.12
X _{sps}		0.04		0.02		0.01		0.02		0.01

931
932

Table 3 cont'd: Compositions of experimental garnets

	15-MORB		15-AMPH		13-GLOSS		12-MORB		11-AMPH	
T (°C)	800		800		850		850		850	
P (Gpa)	2.5		2.5		2.5		2.5		2.5	
time (hr)	48		48		48		48		48	
garnet seed*	Y		Y		Y		Y		Y	
no. analyses	15		15		10		18		13	
	<u>wt %</u>	<u>Q- nrml</u>								
Si**	39.09	2.95	37.38	2.94	36.56	2.93	38.86	2.94	37.90	2.95
SD	0.61	0.05	0.43	0.03	0.32	0.03	0.82	0.07	0.20	0.01
Ti	0.94	0.05	1.37	0.08	2.08	0.13	2.08	0.12	1.59	0.09
SD	0.30	0.01	0.12	0.01	0.13	0.01	0.85	0.05	0.04	0.00
Al	22.45	2.00	20.71	1.92	19.57	1.85	21.20	1.89	20.59	1.89
SD	0.25	0.02	0.23	0.02	0.50	0.04	1.16	0.11	0.21	0.02
Fe	20.34	1.28	28.81	1.89	27.35	1.83	17.51	1.11	24.08	1.57
SD	1.07	0.10	0.45	0.04	0.42	0.03	2.99	0.12	0.27	0.02
Mn	0.46	0.03	0.29	0.02	1.10	0.07	0.35	0.02	0.36	0.02
SD	0.12	0.01	0.09	0.00	0.17	0.01	0.44	0.01	0.13	0.00
Mg	7.41	0.83	3.28	0.38	2.45	0.29	9.58	1.08	6.43	0.75
SD	2.11	0.12	1.61	0.10	0.43	0.02	0.52	0.23	0.48	0.03
Ca	10.49	0.85	9.27	0.78	10.50	0.90	10.14	0.82	9.10	0.76
SD	0.19	0.02	1.07	0.09	0.69	0.06	0.90	0.07	0.28	0.04
	101.17		101.10		99.62		99.72		100.04	
aldef		0.00		0.08		0.15		0.11		0.11
SE		0.02		0.02		0.04		0.11		0.02
Si def		0.05		0.06		0.07		0.06		0.05
SE		0.05		0.03		0.03		0.07		0.01
Al def + 2 Sdef		0.10		0.20		0.28		0.22		0.22
SE		0.02		0.02		0.03		0.06		0.01
ex cat		0.00		0.08		0.11		0.04		0.09
SE		0.16		0.14		0.08		0.27		0.05
X _{grs}		0.28		0.25		0.29		0.27		0.25
X _{alm}		0.43		0.62		0.59		0.37		0.51
X _{prp}		0.28		0.12		0.09		0.36		0.24
X _{sps}		0.01		0.01		0.02		0.01		0.01

933
934

Table 3 cont'd: Compositions of experimental garnets

	14-GLOSS	14-MORB	14-AMPH	14-AMPH 10 kV
T (°C)	900	900	900	900
P (Gpa)	2.5	2.5	2.5	2.5
time (hr)	48	48	48	48
garnet seed*	Y	Y	Y	Y
no. analyses	10	8	9	9
	<u>wt %</u>	<u>O- nrml</u>	<u>wt %</u>	<u>O- nrml</u>
Si**	36.58	2.91	38.69	2.93
SD [⊠]	0.15	0.01	0.00	0.06
Ti	2.16	0.13	1.80	0.10
SD	0.06	0.01	0.00	0.03
Al	19.73	1.85	21.73	1.94
SD	0.32	0.03	0.00	0.05
Fe	25.76	1.72	18.28	1.16
SD	0.67	0.05	0.01	0.11
Mn	1.21	0.08	0.46	0.03
SD	0.07	0.00	0.00	0.01
Mg	3.63	0.43	9.33	1.05
SD	0.45	0.02	0.02	0.26
Ca	10.70	0.91	9.75	0.79
SD	0.21	0.06	0.01	0.12
	99.76		100.04	
				97.50
				99.06
aldef		0.15		0.06
SE		0.03		0.05
Si def		0.09		0.07
SE		0.01		0.06
Al def + 2 Sdef		0.32		0.20
SE		0.01		0.04
ex cat		0.14		0.03
SE		0.08		0.30
				0.17
				0.04
				0.08
				0.03
				0.33
				0.02
				0.02
				0.21
				0.15
				0.15
X _{grs}		0.29		0.26
X _{alm}		0.55		0.38
X _{prp}		0.14		0.35
X _{sps}		0.03		0.01

*indicates if exp. contained Gore Mtn. garnet seeds

**Wt % oxides

***Garnet analyses normalized to 12O

⊠SE is reported in 1σ

935
936

Table 4: Compositions of selected clinopyroxene

	9-GLOSS		15-GLOSS		12-MORB		14-MORB		8-GLOSS	
T (°C)	900		800		850		900		850	
P (Gpa)	1.5		2.5		2.5		2.5		1.5	
	wt. %	O-nrml*	wt. %	O-nrml*	wt. %	O-nrml*	wt. %	O-nrml*	wt. %	O-nrml*
SiO ₂	51.49	3.98	53.67	4.09	52.25	3.88	51.39	3.92	52.81	4.04
SE**	0.52	0.04	0.40	0.03	0.94	0.07	0.35	0.03	2.01	0.15
TiO ₂	0.45	0.03	0.86	0.05	0.61	0.03	0.62	0.04	0.31	0.02
SE	0.09	0.01	0.05	0.00	0.14	0.01	0.05	0.00	0.11	0.01
Al ₂ O ₃	2.86	0.20	4.93	0.33	10.55	0.69	8.04	0.54	2.95	0.20
SE	0.48	0.03	0.48	0.03	0.44	0.03	0.35	0.02	1.46	0.10
FeO	18.41	0.60	13.94	0.44	6.33	0.20	4.69	0.15	16.97	0.54
SE	1.19	0.04	0.86	0.03	1.69	0.05	0.23	0.01	7.45	0.24
MnO	0.48	0.02	0.14	0.00	0.09	0.00	0.06	0.00	0.49	0.02
SE	0.01	0.00	0.04	0.00	0.07	0.00	0.03	0.00	0.13	0.00
MgO	9.09	0.52	7.19	0.41	10.33	0.57	11.96	0.68	9.63	0.55
SE	0.29	0.02	0.31	0.02	0.50	0.03	0.25	0.01	2.28	0.13
CaO	15.31	0.63	14.15	0.58	12.50	0.50	13.52	0.55	14.75	0.61
SE	0.38	0.02	0.40	0.02	0.36	0.01	0.25	0.01	5.87	0.24
K ₂ O	0.28	0.01	0.67	0.02	0.02	0.00	0.02	0.00	0.27	0.01
SE	0.05	0.00	0.03	0.00	0.01	0.00	0.01	0.00	0.20	0.00
Na ₂ O	0.42	0.02	1.92	0.07	3.56	0.13	3.25	0.12	0.39	0.01
SE	0.39	0.01	0.14	0.01	0.52	0.02	0.42	0.02	0.20	0.01
total	98.79		97.46		96.25		93.53		98.58	
X _{Aeg}		0.00		0.00		0.00		0.00		0.00
X _{Jd}		4.73		19.71		34.01		30.31		4.54
X _{Di}		95.27		80.29		65.99		69.69		95.46

*normalized to 6O

**SE are reported in 1σ

937

Table 5: Selected glass compositions, normalized to anhydrous totals

	10_GLOSS	10_AMPH	10_MORB	8_GLOSS	9_GLOSS	13_GLOSS	14_AMPH	14_GLOSS
SiO ₂	75.64	72.31	72.72	73.12	68.46	77.75	66.09	74.42
SE*	0.66	0.55	1.67	1.18	0.75	2.46	3.91	1.43
TiO ₂	0.24	0.25	0.27	0.37	0.66	0.46	0.54	0.57
SE	0.02	0.02	0.07	0.04	0.01	0.04	0.06	0.05
Al ₂ O ₃	13.90	16.34	17.29	13.82	14.33	11.69	17.33	11.54
SE	0.14	0.19	1.09	0.10	0.10	0.66	2.10	0.21
FeO	2.32	2.55	1.97	4.43	6.55	2.29	4.65	3.96
SE	0.25	0.89	0.93	0.32	0.22	0.83	1.38	0.34
MnO	0.03	0.00	0.03	0.10	0.19	0.03	0.03	0.06
SE	0.02	0.18	0.02	0.03	0.01	0.02	0.02	0.02
MgO	0.33	0.21	0.40	0.60	1.08	0.20	0.56	0.44
SE	0.04	0.18	0.36	0.06	0.04	0.12	0.31	0.03
CaO	3.05	1.88	2.79	3.89	4.99	1.51	2.97	2.58
SE	0.16	0.23	1.37	0.15	0.30	0.23	1.89	0.46
K ₂ O	3.16	2.20	1.67	2.62	2.50	3.73	1.94	3.99
SE	0.12	0.04	0.72	0.26	0.10	0.29	0.24	0.19
Na ₂ O	1.32	4.26	2.87	1.03	1.23	2.34	5.88	2.44
SE	0.26	0.76	0.78	0.18	0.21	0.43	0.45	0.25
total	89.44	92.37	88.83	89.34	88.85	87.80	89.83	87.54
FM	1.09	1.12	0.95	1.44	1.98	1.18	1.74	1.72

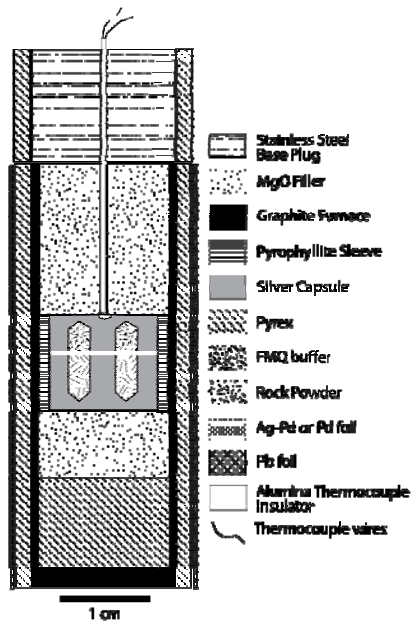
*SE are reported in 1σ

938
939

941

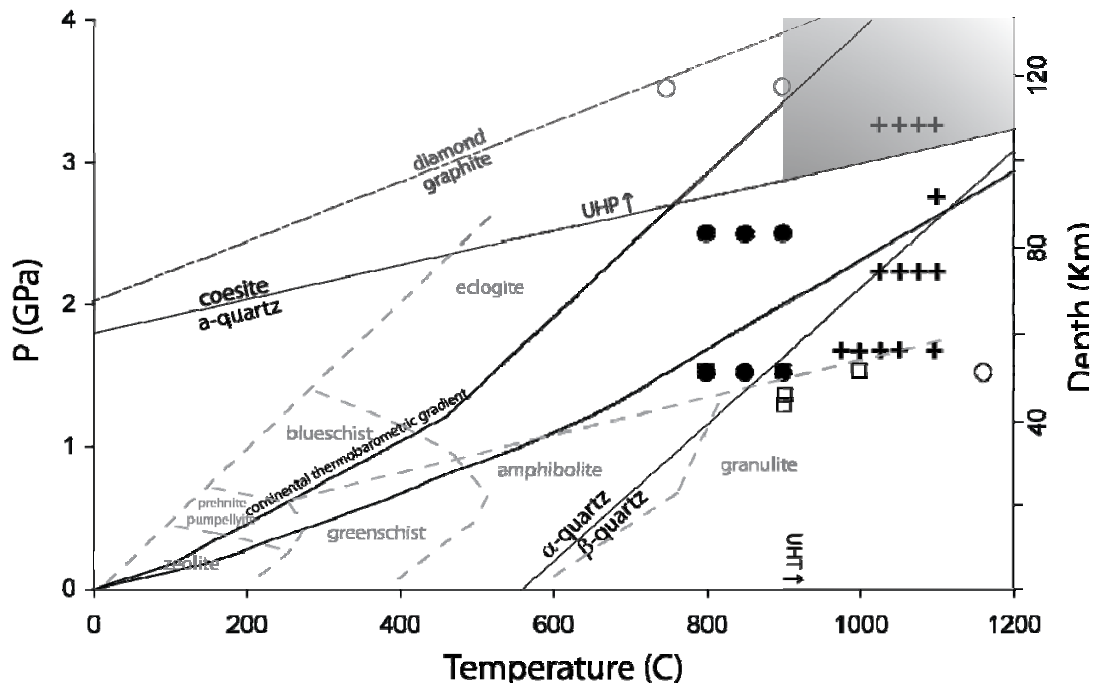
Figures

942 **Figure 1**



943

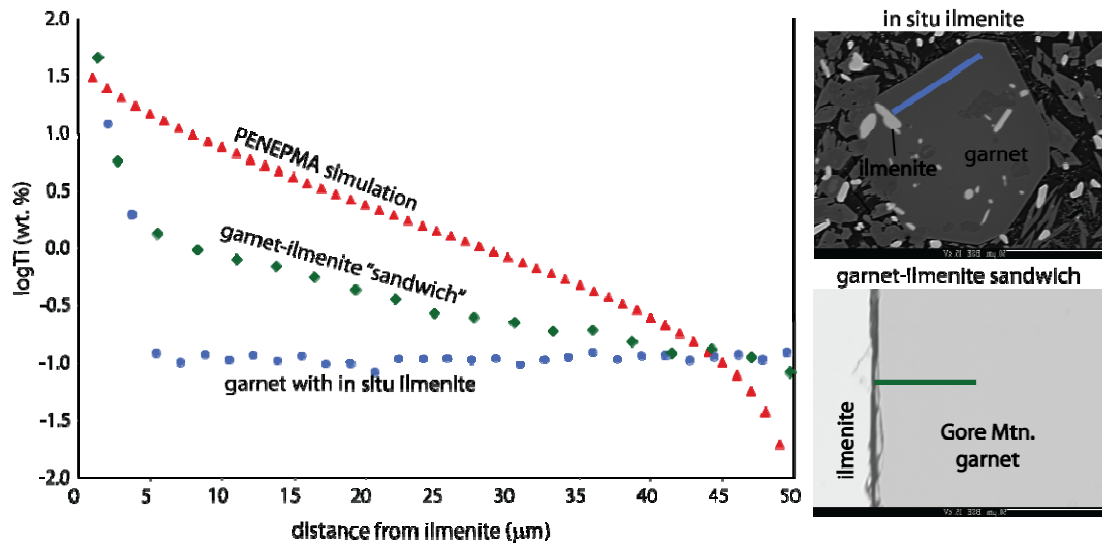
944 **Figure 2**



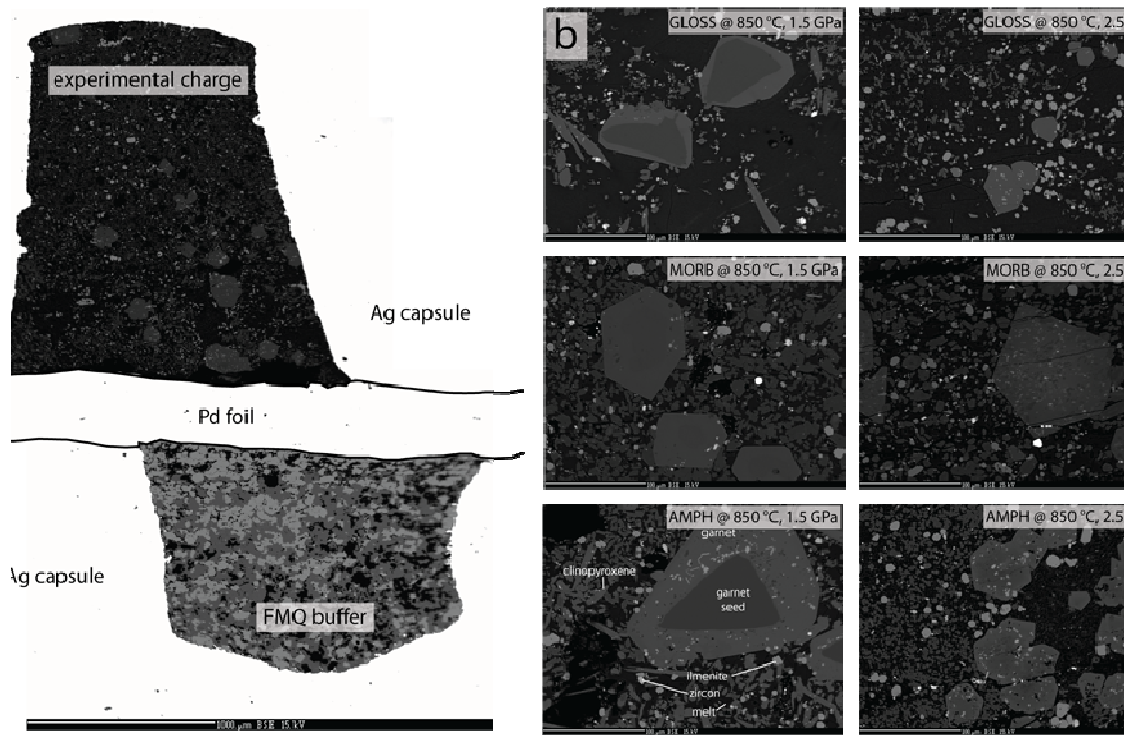
945

946

947 **Figure 3**

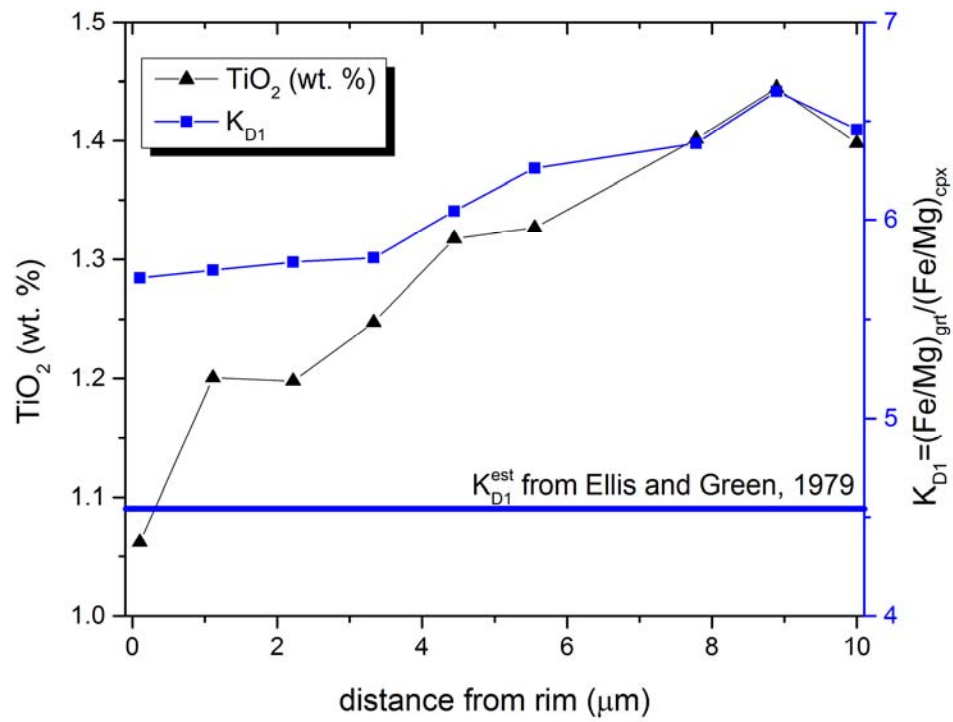


948 **Figure 4**
 949



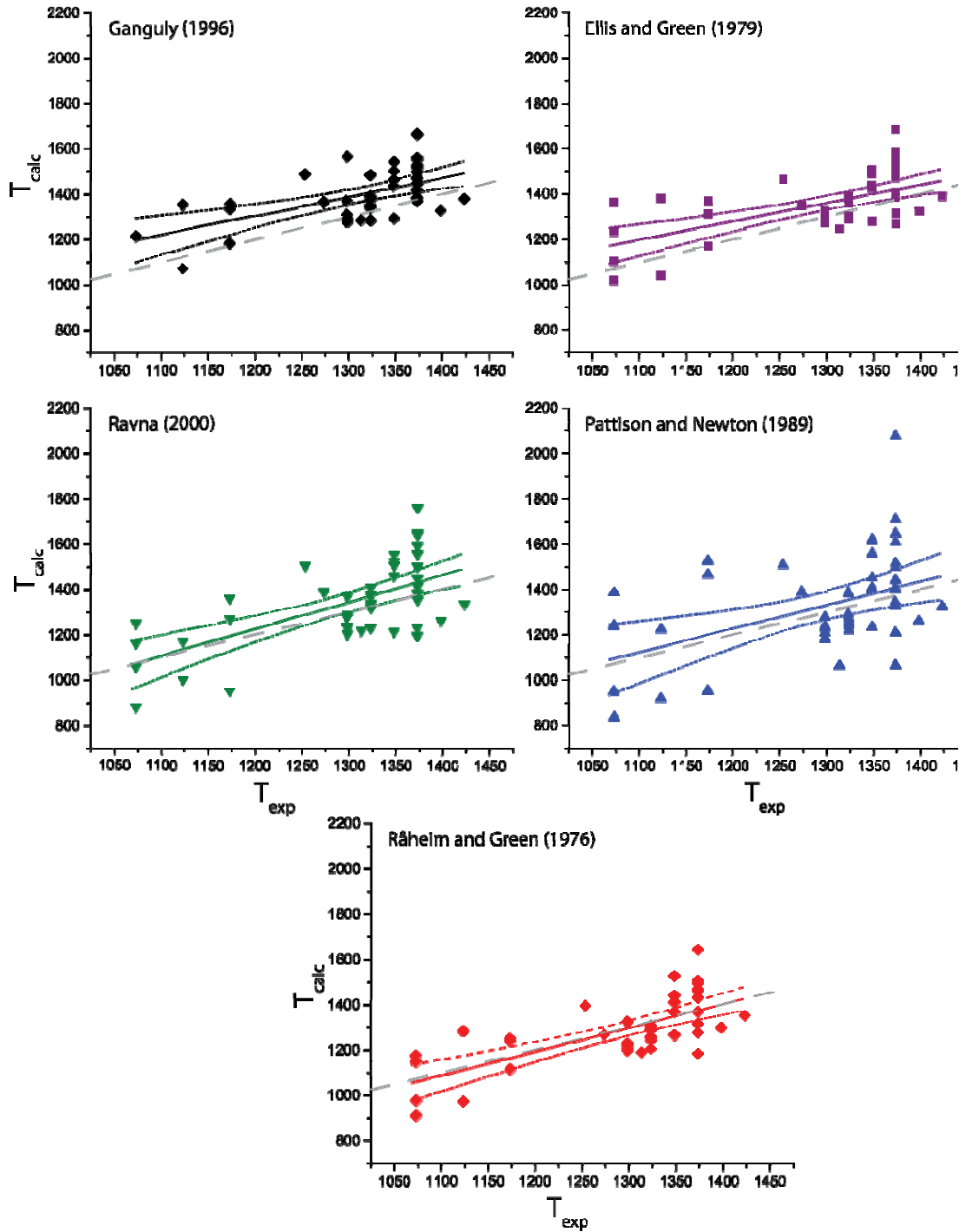
950
 951

951 **Figure 5**



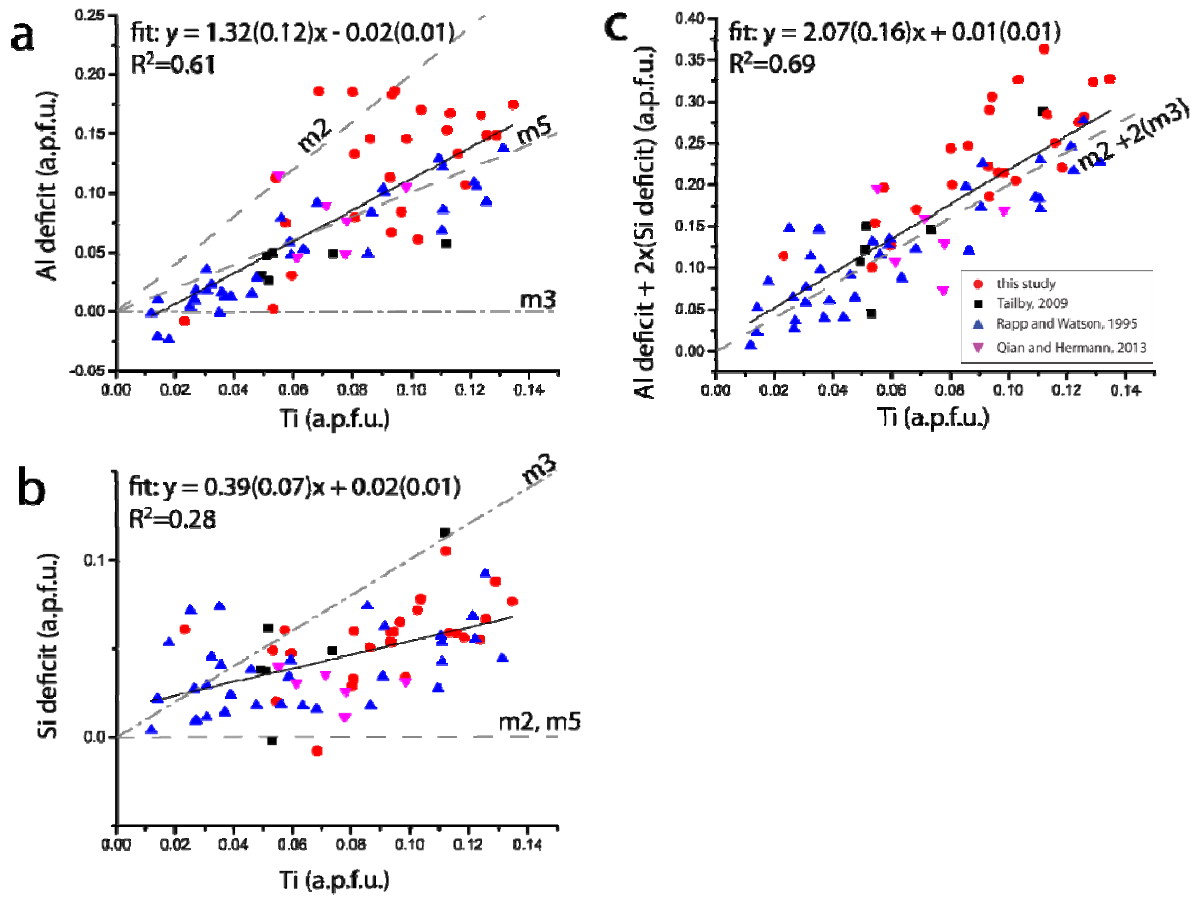
952
953

955 **Figure 6**
956



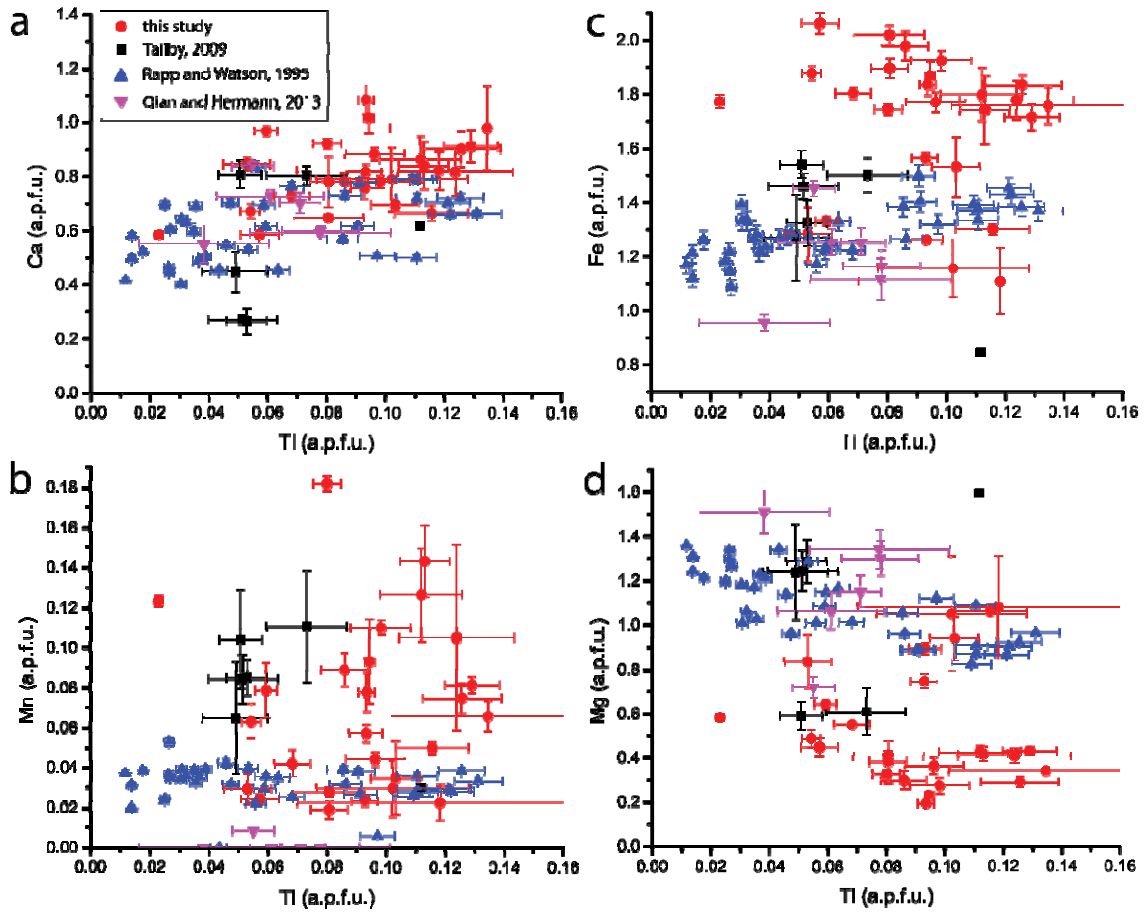
957
958

959 **Figure 7**



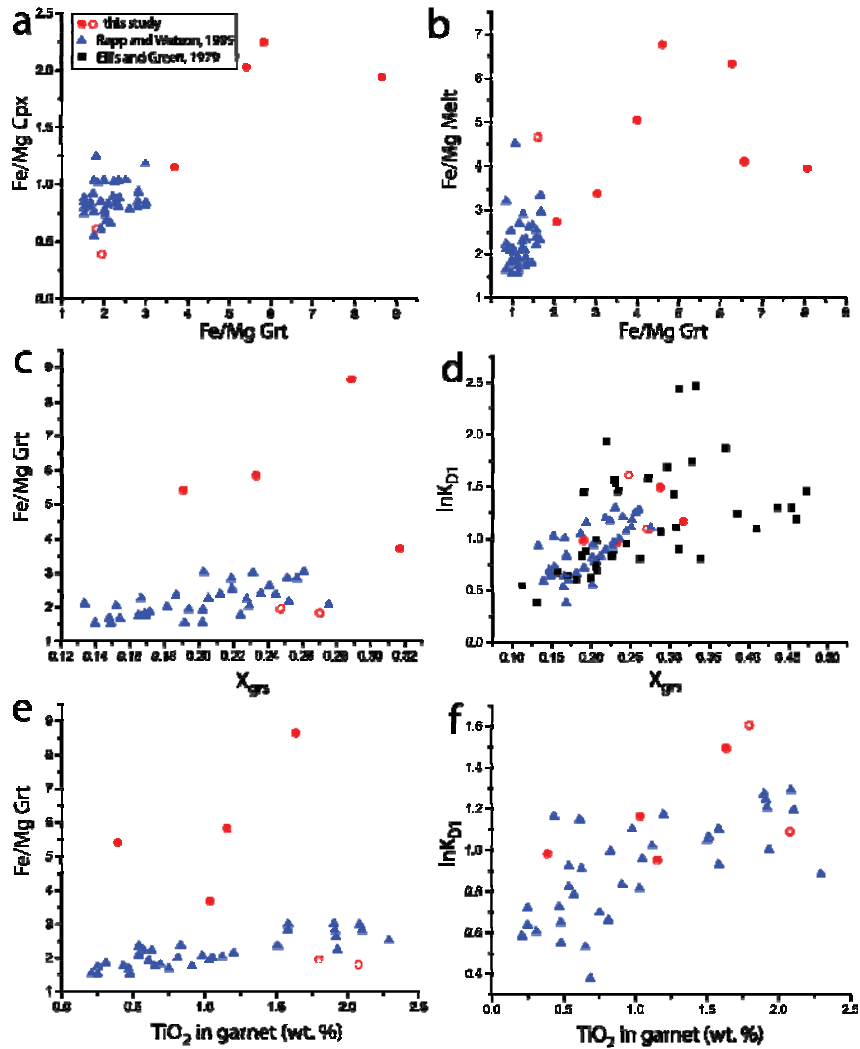
960
961

962 **Figure 8**



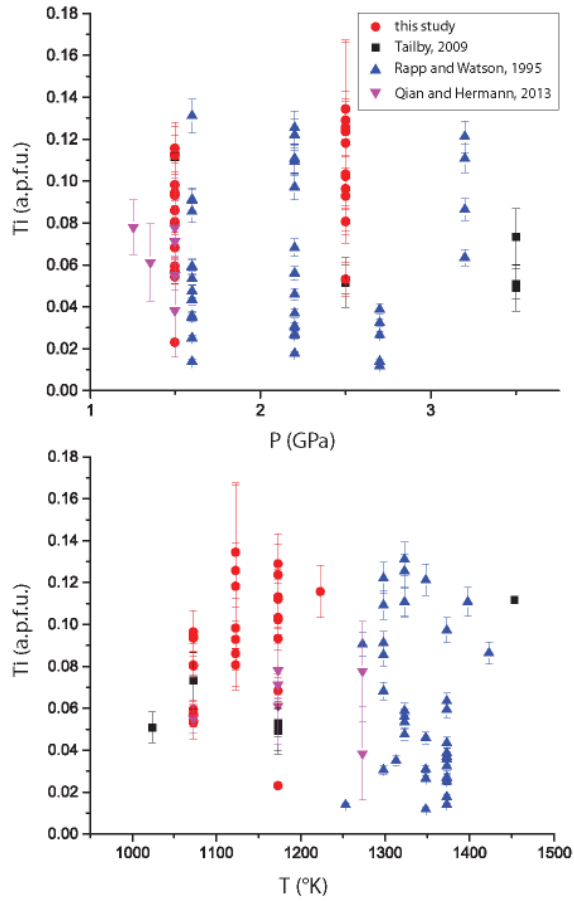
963
964

965 **Figure 9**

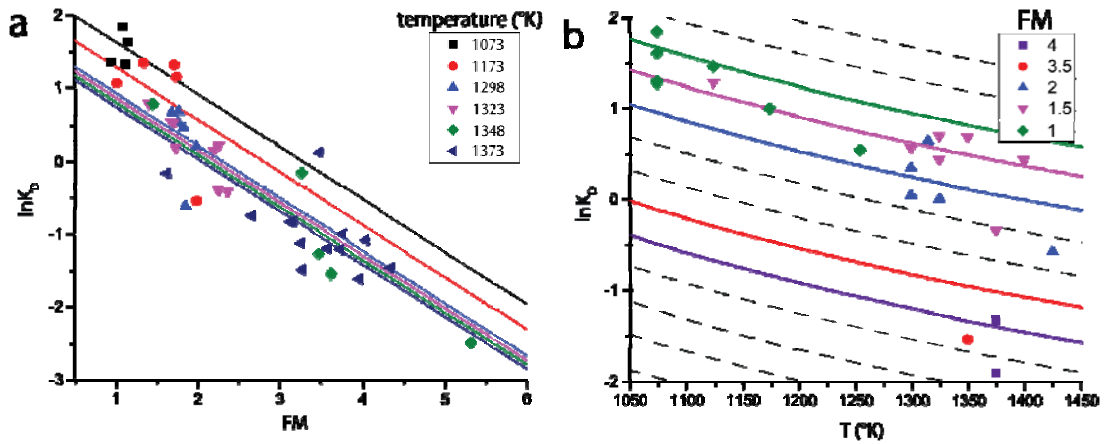


966
967

968 **Figure 10**

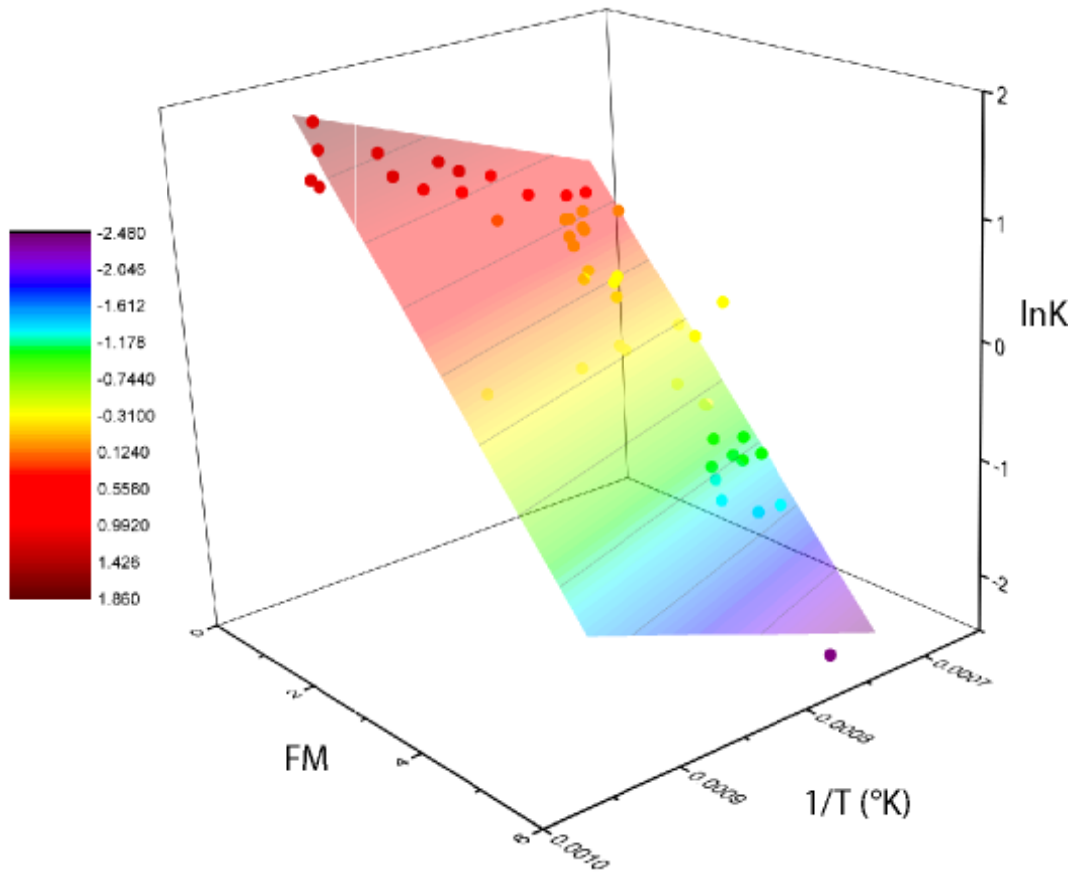


969
 970 **Figure 11**



971
 972

973 **Figure 12**



974
975

976 **Figure 13**

